# Increase in Carbon Monoxide (CO) and Aerosol Optical Depth (AOD) observed by satellite in the northern hemisphere over the summers of 2008-2023, linked to an increase in wildfires

Antoine Ehret[1], Solène Turquety[1], Maya George[1], Juliette Hadji-Lazaro[1], and Cathy Clerbaux[1,2]

[1]LATMOS/IPSL, Sorbonne Université, UVSQ Université Paris-Saclay, CNRS, Paris, France
[2]Spectroscopy, Quantum Chemistry and Atmospheric Remote Sensing (SQUARES), Université Libre de Bruxelles (ULB), Brussels, Belgium

**Correspondence:** Antoine Ehret (antoine.ehret@latmos.ipsl, fr)

**Abstract.** Biomass burning has a significant impact on the composition of the atmosphere and climate due to large emissions of trace gases and aerosols. Previous studies have demonstrated the influence of biomass burning emissions on the spatial and temporal variability of carbon monoxide (CO) and aerosols concentration on hemispheric scales. This study aims to examine the variability of fires and their impact on the mean and extreme values of CO and aerosol optical depth (AOD) observed by satellite (IASI/Metop for total column CO and MODIS/Terra and Aqua for AOD), focusing on the extratropical Northern Hemisphere (NH) from 2008 to 2023. While biomass burning due to agricultural practices is decreasing in many regions, boreal regions and the western United States have experienced a notable rise in burned area, up to +37 % in recent years (2017–2023) compared to the 2008–2023 period, and fire intensity. This is consistent with an increase in meteorological fire risk in these regions. The increase in wildfires has led to a rise in the mean and extreme values of CO and AOD during the summer and early autumn across all NH, up to +9.3 % and +33 % for extreme values of total column CO and AOD in boreal regions and the western United States in recent years compared to 2008–2023. The number of days with extreme total column CO and AOD has increased by more than 50 % in recent years during summer in North America, the Atlantic and Europe, in comparison to the full period. A robust correlation (r=0.83) between the number of plumes and burned areas in the extratropical northern hemisphere is obtained.

## 1 Introduction

Biomass burning is a significant source of trace gases, including greenhouse gases, and aerosols (Andreae and Merlet, 2001; Andreae, 2019), contributing to climate forcing and atmospheric pollution. On a global scale, Johnston et al. (2012) estimate that it caused 260,000 to 600,000 premature deaths each year over the period 1997–2006. Exposure to pollution from biomass burning leads to a significant increase in mortality, of the order of 4 % (all-cause mortality, cardiovascular mortality and

respiratory morbidity) for a $10\,\mu g\,m^{-3}$ increase in the concentration of fine particles (PM2.5, diameter $\leq 2.5\,\mu m$) (Karanasiou et al., 2021). During intense wildfires, PM2.5 concentrations can increase by several hundred $\mu g\,m^{-3}$ over large areas, with a major health impact (Xu et al., 2020; Chen et al., 2021a). Studies show that wildfires may be more harmful than other sources, due to the toxicity of particulate matter and the cocktail effect of co-exposure to high temperatures and to other air pollutants, including ozone (e.g. Keywood et al., 2015; Aguilera et al., 2021).

Historical reconstructions show that fire-related carbon emissions have been stable since the pre-industrial era on a global scale (van Marle et al., 2017). The emissions are largely controlled by fires in Africa (more than half of global emissions) and tropical regions of America an Asia (almost 25 % of emissions) (van Marle et al., 2017), where the long term evolution of biomass burning is linked to changes in land use (Andela et al., 2017). Based on satellite observations of fire activity, Chen et al. (2023) show that global burned area decreased by approximately 22 % between 1997 and 2020, driven by a decrease in tropical north Africa, northern Australia, Southern Hemisphere South America, and the Eurasian Steppe. However, burned areas tend to increase in the mid and high latitudes of the Northern Hemisphere.

The extent of a wildfire after ignition depends on the availability of fuel and weather conditions (e.g., hot and dry conditions being favourable to propagation). Weather conditions drive the inter-annual variability in burned area and season length in the Mediterranean area, the western USA and the high latitudes of the Northern Hemisphere (Jones et al., 2022). In these regions, fire weather indexes derived from surface temperature, relative humidity, precipitation and wind speed, have been shown to be well correlated with observed fire activity (Grillakis et al., 2022) and are widely used to study the evolution of the vulnerability to wildfire. These studies have highlighted a significant lengthening of fire seasons in many regions since 1979, accompanied by an increased probability of long fire seasons (Jolly et al., 2015). An increase in extreme conditions, and extreme fire activity, is attributed to surface temperature increase and associated water deficit due to evaporation, rather than a decrease in precipitation (Jain et al., 2022; Jones et al., 2022). With the increasing intensity of wildfires, the impact on regional air quality is also becoming more severe, and is projected to increase in the context of climate change (Ford et al., 2018; Tian et al., 2023).

The anthropogenic origin of most wildfires in temperate regions offers potential for mitigating their effect. Indeed, human-initiated fires account for more than 80 % of population exposure to fire PM2.5 in the US (Carter et al., 2023) and over 96 % of the fires in the European Union are caused by humans (San-Miguel-Ayanz et al., 2024). In boreal regions however, a significant fraction of wildfires, more than 80 % of burned area in North American boreal forests between 1975 and 2015, are triggered by lightning strikes (Veraverbeke et al., 2017). They often affect remote areas and burn for many weeks, sometimes smoldering throughout the winter (Scholten et al., 2021). Their effect on atmospheric composition is major, and likely to intensify in coming years (Chen et al., 2021b; Hessilt et al., 2022).

In addition to local effects on air quality, the large smoke plumes emitted by the most severe wildfires may be transported over long distances, altering air quality at continental scales, sometimes hemispheric scale. Several studies have shown that emissions from biomass burning control the interannual variability of both carbon monoxide (CO) and aerosol concentrations (e.g. Szopa et al., 2007; Spracklen et al., 2007; Jaffe et al., 2008). CO is emitted by incomplete combustion from anthropogenic ($\sim 60$ % of direct emissions) and biomass burning sources. It is also produced by the oxidation of methane and volatile organic

compounds. This secondary production accounts for almost half of the CO sources (Zheng et al., 2019). Its main sink is its oxidation by the hydroxyl radical (OH), which is larger in summer, resulting in a shorter lifetime of CO, and lower CO values. However, its lifetime remains relatively long, several weeks during summer, which allows transport on long distances. During intense wildfires, large amounts of CO are emitted, resulting in large CO plumes transported over hundreds to thousands of

60  kilometers. The plumes exhibit CO concentrations that are well above background values. It is therefore considered a reliable proxy of biomass fire smoke plumes.

Aerosols have a large variety of emissions and precursors, as well as a shorter lifetime (in particular due to rapid deposition) but combustion is also a large contribution to the total loading. Both CO and aerosol optical depth (AOD) are well observed by satellite, allowing a monitoring of wildfire plumes transport and impact (e.g. Edwards et al., 2004; Turquety et al., 2020;

65  Buchholz et al., 2021; Albores et al., 2023; Ceamanos et al., 2023). On longer time scales, the availability of satellite observations of CO and AOD since the early 2000s allows the analysis of observed trends. Both AOD and surface PM concentrations show a decrease in aerosol load since 2000 over the mid-latitudes of the Northern Hemisphere, especially over Europe, North America and, since 2010, over China (Intergovernmental Panel On Climate Change, 2023), that may be attributed to a decline in anthropogenic emissions due to the implementation of air quality management policies, and better combustion efficiencies.

70  As for AOD, the decrease in total column CO is particularly marked over eastern Asia and the northern Pacific (Zheng et al., 2018). Using inverse modeling, Zheng et al. (2019) attribute the decreasing trends in 2000–2017 to decreasing anthropogenic emissions in the United States, Europe and in China, but also to decreasing biomass burning emissions, especially in equatorial Africa. Over areas influenced by wildfires, observations show a compensation of the general downward trend observed for CO over the past decade, especially in late summer (Buchholz et al., 2021, 2022). Similar results are obtained for particulate matter

75  (O'Dell et al., 2019).

In this context, this study aims to examine the variability of fires and their impact on the atmospheric composition in the Northern Hemisphere between June and October for the 2008–2023 period. Fire activity is characterised using fire observations by the MODIS instrument (active fires and burned area products) in terms of both burned areas and fire intensity (using the fire radiative power as proxy). The Canadian Fire Weather Index (FWI) is used to analyse whether the observed evolution

80  of wildfires may be attributed to weather conditions more or less prone to fire spread or whether it is due to human activity. The resulting wildfire plumes are identified and characterised using satellite observations of CO and AOD from the IASI/Metop, MODIS/Terra and MODIS/Aqua instruments during the period 2008–2023. The study is focused on the boreal summer (June to October), which corresponds to the fire season in the extratropical regions and minimises the long-range transport of anthropogenic pollution, more specifically the maximum export from Asia in Spring.

85  The data and methods used for this study are described in section 2. After a presentation of the general characteristics of fire activity in the Northern Hemisphere (section 3.1), the trends (section 3.2) and recent anomalies (section 3.3) in fire activity are analyzed. A more specific focus on the evolution of the Fire Weather Index is presented in section 3.4. The variability of the means and extremes of total column CO and AOD is investigated in section 4.1. In a similar approach to that adopted for fire activity, the trends (section 4.2) and recent anomalies (section 4.3) in total column CO and AOD are examined. Finally, the

90 evolution of the impact of wildfires is characterized in terms of the number of days with plumes of extreme values of CO and AOD over different regions of the Northern Hemisphere (sections 4.4).

## 2 Data & Methods

### 2.1 Observations of fire activity

The analysis of fire activity is conducted using the MODIS Collection 6 databases (Giglio et al., 2018). The burned area is cal-
95 culated based on the MCD64A1 product, which provides the date of burning at a resolution of 500 m (Giglio et al., 2010, 2015). The active fire products MOD14 and MYD14, based on thermal anomalies, are employed for retrieval from MODIS observations onboard Terra (equator crossing time 10:30 LST) and Aqua (equator crossing time 13:30 LST), respectively. These products provide the date of burning at a 1 km resolution as well as the fire radiative power (Giglio et al., 2006). The fire radiative power represents the energy released during combustion and measures the intensity of a biomass fire (Wooster and
100 Zhang, 2004). A linear relationship exists between the burned area and the fire radiative power, up to a certain limit depending on the region and vegetation burned. Beyond this limit, the burned area tends to flatten or decrease with increasing fire radiative power (Laurent et al., 2019).

Both burned area and active fires are processed using the APIFLAME v2.0 software (Turquety et al., 2020). If a fire is detected at a given date, the assumed burned area is calculated as the size of the pixel, modulated by the fraction of the pixel
105 covered by vegetation.

In both cases, only data of the highest confidence are employed (based on quality flags). The main source of uncertainty is associated with cloud cover, which masks surface anomalies. The temporal resolution that can be achieved (i.e. the uncertainty on the date of burning) is estimated to be approximately two days (Giglio et al., 2018). The horizontal resolution of the MODIS detection is 500 m for the burned area product and 1 km for the active fires product. This may result in an overestimation of the
110 burned area in some cases.

In the case of active fires, false detections that may be associated with industrial activity, for instance, are also filtered using a statistical analysis (as described in Turquety et al., 2020). A large number of active fires remain in the Persian Gulf, and therefore it has been deemed appropriate to mask them in order to avoid the occurrence of false positives due to oil and gas operations. It is important to note that the MCD64A1 product may be less effective in detecting smaller fires, which are more
115 easily identified by their thermal signature, resulting in an underestimation of the burned area (Randerson et al., 2012; Ramo et al., 2021). New products based on finer-resolution satellite instruments and taking better account of small fires estimate a global burned area that is between 43 % and 93 % greater than that estimated by MCD64A1 (Chen et al., 2023; Lizundia-Loiola et al., 2022).

The daily burned area and fire radiative power datasets derived from MODIS are gridded on a 0.5°×0.5° grid covering the
120 Northern Hemisphere, which facilitates the analysis.

In consideration of the fact that a fire can persist for several consecutive days, a database of detected events is constructed. A fire event in a grid cell is defined as one or more consecutive days with at least one fire detected in the grid cell and a

total burned area greater than 50 ha. This threshold was selected in order to focus on events that contribute significantly to the regional burned area and to discard detections that are isolated in space and time. The aforementioned definition may result in the splitting of long fire events into several shorter events due to the occurrence of extended cloud cover. However, the relatively large horizontal resolution of 0.5° often results in the aggregation of several smaller events into a single one. We thus have chosen not to allow missing days in between events.

## 2.2 Satellite observations of CO

The CO observations from the IASI/Metop instrument, launched in 2006 on board Metop-A, 2012 on board Metop-B and 2018 on board Metop-C, are used. The IASI instrument measures the outgoing thermal infrared radiation in a nadir-viewing geometry twice daily (equator crossing time 9:30 LST). The swath of 2200 km across nadir allows for global coverage twice daily with a pixel size of $\sim 12$ km diameter at nadir (Clerbaux et al., 2009). The CO columns are obtained from the CO partial column profiles retrieved from the IASI spectra (Hurtmans et al., 2012), reprocessed backward in time by Eumetsat (CO CDR http://doi.org/10.15770/EUM_SAF_AC_0047) to provide a consistant climate record from 2008 to 2023. Only IASI CO observations containing less than 25 % cloud cover are taken into account in the CO inversion for IASI CO CDR data. The corresponding degrees of freedom for the signal, which characterise the independent information on the vertical, vary between 0.8 and 2.4. The maximum sensitivity is observed in the free troposphere ($\sim$ 5–7 km), while the sensitivity to the surface layers is strongly dependent on the thermal contrast (Clerbaux et al., 2009).

The use of CO CDR data avoids introducing bias due to the use of different versions of the retrieval algorithm over time, which would be a problem for the analysis of long term time series as shown by Barret et al. (2025).

Comparisons between IASI CO CDR L2 and NDACC FTIR data are performed for 23 stations in (Langerock, 2023). Relative differences are ranging between -3.75 % (-4.17 %) for Zugspitze to 15.09 % (15.01 %) for Toronto, for IASI-A (B). The mean bias for the 23 stations is 3.89 % for IASI-A and 4.19 % for IASI-B. Barret et al. (2025) estimated, for a version of FORLI-CO (v20151001) older than CO CDR used here, a mean bias of -6 % for IASI-A CO total column compared to IAGOS CO total column.

For the purposes of this study, only daytime total columns (larger degrees of freedom and sensitivity to the lower troposphere than night-time observations), with a general quality flag superior or equal to one are considered. Since this work only evaluates total column CO, "total column CO" will be designated as "CO".

## 2.3 Satellite observations of AOD

In order to analyse aerosol plumes, the MODIS collection 6.1 Level 2 products (MOD04_L2 for Terra http://doi.org/10.5067/MODIS/MOD04_L2.061, and MYD04_L2 for Aqua http://doi.org/10.5067/MODIS/MYD04_L2.061) are used, combining the dark target and deep blue data (Levy et al., 2013, 2015). More specifically, the AOD at 550 nm and 10 km horizontal resolution, with good to very good confidence level, is used. The uncertainty is estimated to be ±(0.05+0.15 AOD) for the dark target product, ±(0.03+0.20 AOD) for the deep blue product, and -0.01 bias for the merge product (correlation of 0.86 compared to surface remote sensing) (Sayer et al., 2014).

As for the fire products, both CO and AOD products are gridded on a 0.5°×0.5° grid covering the Northern Hemisphere.

## 2.4 Fire weather index

The Canadian Fire Weather Index (FWI) is computed using ERA5 high-resolution reanalysis (0.25° resolution), including overwintering, as detailed in Van Wagner (1987); McElhinny et al. (2020). The parametric model is constrained using the temperature, relative humidity and wind at 12:00 LST and the cumulated precipitation during the last 24 hours. Three indices are derived to characterise fire behaviour: the initial spread index, the build-up index and the fire weather index. In this instance, the fire weather index is used and regridded onto the 0.5°×0.5° resolution Northern Hemispheric grid.

## 2.5 Extremes and plume identification

To study the impact of fires on the atmospheric composition, this study focuses on the average and extreme values of CO and AOD between June and October for the 2008-2023 period. In addition, the average and extreme values of the FWI are used in the analysis of fire variability. Among the extreme values of CO and AOD, intense plumes from forest fires are identified, thereby enabling the linkage of the variability of fire activity and the variability of atmospheric composition.

For each variable $X$ (i.e., CO, AOD or FWI) analyzed and each grid cell $i$, the extremes are quantified using the 97th percentile ($Q_{97,X}(i)$), which is calculated using the percentile of the distribution of values in the grid cell over a fire season (June–October) during the study period (2008–2023).

Using this definition of extreme values of CO and AOD, intense plumes transported from major wildfires can be identified based on a percentile limit anomaly. The spatial extent of plumes is assessed using boxes of size 20°×24°, with each box containing an identical number of 0.5° grid cells. These boxes are arbitrarily defined beforehand, with the northern hemisphere subdivided into 60 boxes. Consequently, if $X$ represents the variable under consideration (e.g. CO or AOD) in grid cell $i$, a percentile limit anomaly is calculated as $PLA97_X(i) = X(i) - Q_{97,X}(i)$. A plume is identified if $PLA97_X(i) > 0$ on more than 5 % of the grid cells in the box and for at least two days. Therefore, values of CO or/and AOD within a given region are considered to be indicative of intense plumes transported from major wildfires when these values are extreme, i.e. well above the background level, for two consecutive days and when they are close to a set of extreme values. This definition enables the number of false detections to be minimized by not considering extreme values with limited spatial and temporal extents as plumes from intense fires.

## 2.6 Trends and recent evolution

This study examines the trends and recent evolution of burned area, fire weather index, CO and AOD between 2008 and 2023 in the Northern Hemisphere.

The Mann-Kendall non-parametric trend test is employed to compute trends in the time series (Hussain and Mahmud, 2019). A trend is considered significant when the p-value is less than 0.1. To focus on the peak of the fire seasons, trends are calculated for the 16-year time period 2008–2023 for variables integrated over both the entire year and over the June to October period.
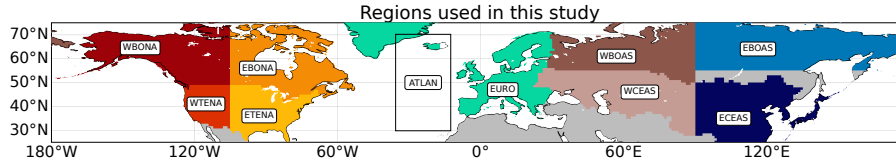
**Figure 1.** Regions used to analyse the variability and trends in fire observations : Western Boreal North America (WBONA), Western Temperate North America (WTENA), Eastern Boreal North America (EBONA), Eastern Temperate North America (ETENA), Europe (EURO), Western Boreal Asia (WBOAS), Western Central Asia (WCEAS), Eastern Boreal Asia (EBOAS), Eastern Central Asia (ECEAS). The region above the Atlantic (ATLAN) is used to analyse the variability and trends in CO and AOD. The grey areas correspond to regions not analyzed in this study.

Trends in both mean and extreme values (97th percentile) are calculated for each 0.5° grid cell, and for the larger regions mapped on Fig. 1. These regions were chosen to represent the main regions prone to wildfires (see sub-section 3.1) and to be consistent with the literature on the subject (e.g. Jones et al., 2022). In order to evaluate trends in pollution transport, an additional region above the Atlantic Ocean is considered.

Since 2017, wildfires in North America have been particularly intense (e.g. Parisien et al., 2023). In order to evaluate the evolution in recent years compared to the full time-series, absolute and relative differences between the variables observed during the recent years (7 years, 2017–2023) and the whole time period with consistent observations (16 years, 2008–2023) are calculated. The decision to use values averaged over the entire 2008–2023 period as reference, as opposed to the 2008–2016 period, is motivated by the objective of employing the most extensive time series possible. Additionally, the selection of the recent period (2017-2023) is visually determined from the temporal variation of fires in the middle and high latitudes of the Northern Hemisphere. The selection of the 2008–2016 period for the calculation of anomalies would result in an increase in the bias associated with the choice of recent period. Finally, the anomalies are expected to be higher when calculated using values averaged over the 2008–2016 period as opposed to the 2008–2023 period. For instance, the recent anomaly of the IASI CO in Europe is 1.6 % when calculated using $(\overline{X_{2017-2023}} - \overline{X_{2008-2023}})/\overline{X_{2008-2023}}$ and is 2.9 % when calculated using $(\overline{X_{2017-2023}} - \overline{X_{2008-2016}})/\overline{X_{2008-2016}}$. Consequently, our choice is a conservative one. The significance of the difference between $\overline{X_{2017-2023}}$ and $\overline{X_{2008-2023}}$ is calculated using an unequal variances t-test. A difference is considered significant when the p-value is less than 0.1.

Variations in the annual total (burned area) or average (fire radiative power, fire weather index, CO and AOD) are calculated, as well as variations over four different time periods: June–October (full season), June–July (early season), July–August (middle season) and September–October (late season).

Subsequent analysis will demonstrate that the calculated differences are of minimal significance. This can be attributed to two factors: firstly, the limited time series available (16 years); and secondly, the calculation method employed, which considers the difference between the recent years (2017–2023) and the entire time series (2008–2023). This approach reduces the significance of the difference, as the two periods are not disjoint. Nevertheless, the examination of recent changes offers supplementary insights to the study of trends, as it highlights the impact of recent years on the variables studied.

# 3 Results on variability and trends in fire activity

## 3.1 General characteristics

The general characteristics of fire activity differ between regions of the Northern Hemisphere. The total monthly burned area in the regions of Fig. 1 is shown in Fig. A1. In most regions, the period June through October corresponds to the peak of the wildfire season, and consequently of observed monthly burned area. However, in several regions (Eastern Temperate North America ETENA, Western Boreal Asia WBOAS, and Eastern Central Asia ECEAS), large burned area, frequently higher than in summer, are observed during spring. These fires will not be taken into account in this study, which focuses on summer variability.

Figure 2 shows the total annual June-October burned area in the Northern Hemisphere, averaged for years 2008–2023, as well as the total mean fire radiative power during June–October, the fraction of years when a fire was detected in each grid cell and the mean length and size of fire events.

Three types of region can be distinguished:

1. Human-managed fire regions : regions with high June–October total burned area, frequent fire detection (almost at least one fire event per gridcell per year) , low mean June–October fire radiative power and small average burned area per fire event, such as eastern Europe, western central Asia or the south-eastern United States, suggesting agricultural burning (post-harvest crop residue burning and field clearing before planting) and/or controlled burn for land management (Hall et al., 2024).

2. Wildfire regions : regions with large June–October total burned area, high frequency (more than at least one fire event per gridcell every two years), large mean June–October fire radiative power and large average burned area per fire event, such as California and the Iberian Peninsula, and strong inter-annual variability;

3. Remote wildfire regions : regions with low frequencies but large total burned area during June–October and large mean June–October fire radiative power, relatively long fire events (thus a large average burned area per fire event), suggesting extreme events and strong inter-annual variability, such as in the high latitudes of the Northern Hemisphere.

In order to facilitate the reading of the manuscript, the decision was taken to concentrate on the regions where fires are most intense and where extreme smoke plumes are most likely to originate. The Eastern Central Asia region was retained due to its significant contribution to the levels of pollutants in the Pacific. To simplify the analysis, regions identified as "human-initiated fire regions" where fires do not appear to cause extreme smoke plumes as defined by our method, have been excluded. Consequently, the regions of primary interest (Fig. 1) are Western Boreal North America, Eastern Boreal North America, Western Temperate North America, Europe, Eastern Boreal Asia, as well as Eastern Central Asia region. Limiting the analysis to the months of June through October should allow us to address the majority of uncontrolled fires, but it will also include the contribution from land management and agricultural burning in some regions.
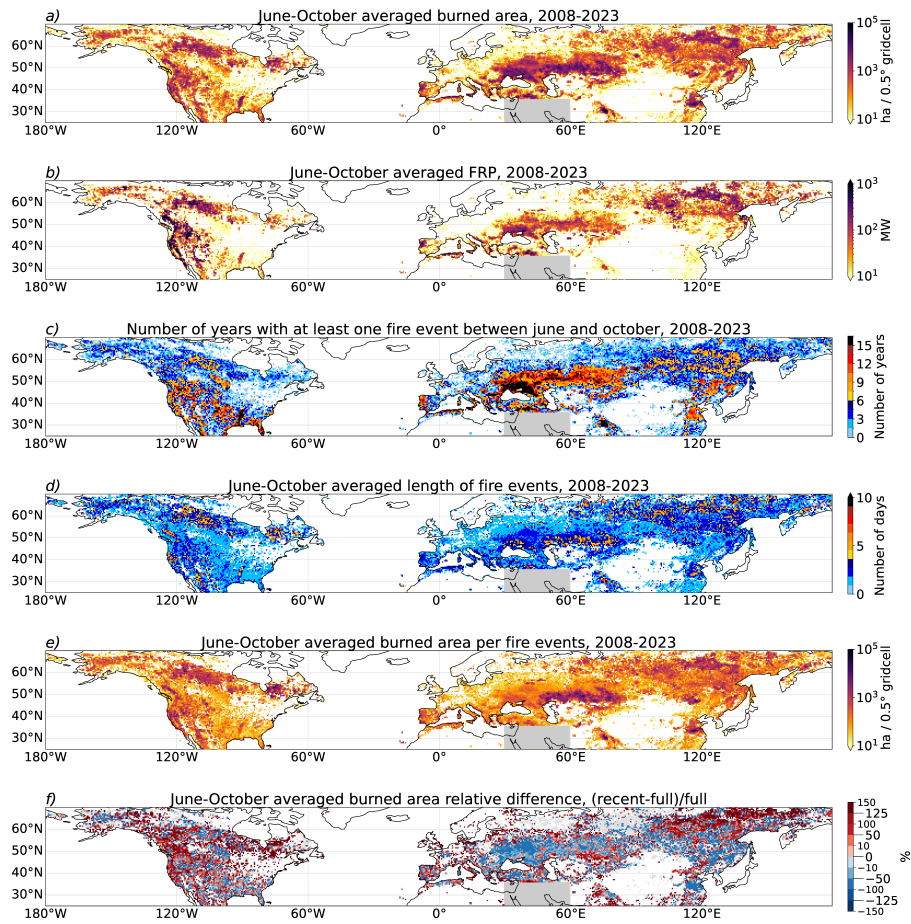
**Figure 2.** (a) Total burned area during June–October derived from MODIS observations, for years 2008–2023. (b) Mean fire radiative power (FRP) during June–October derived from MODIS observations, for years 2008–2023. (c) Number of years with at least one fire event between June and October, for years 2008–2023. (d) June–October averaged length of fire events, for years 2008–2023. (e) June–October averaged burned area per fire event, for years 2008–2023. (f) Relative difference between June–October burned area during recent years (2017–2023) and the full period (2008–2023). Grid cells in green indicate areas that were affected by fires exclusively during the 2017–2023 period, while grey cells indicate areas that were affected by fires exclusively during the 2008–2016 period. The difference is calculated as (recent-full)/full. All variables are averaged on a 0.5°×0.5° grid. Given the considerable number of active fires associated with oil and gas operations in the Persian Gulf, it has been deemed appropriate to mask them with a grey rectangle.

## 3.2 Trends in fire activity during 2008–2023

Due to the large variability in the location and timing of fires, the evaluation of trends in fire activity is conducted at the regional level (regions of Fig. 1), rather than at the grid cell level. Figure 3 illustrates the annual and seasonal variations of the burned area in selected regions of interest and/or showing significant trend. The results are presented in Table 1 for selected regions.
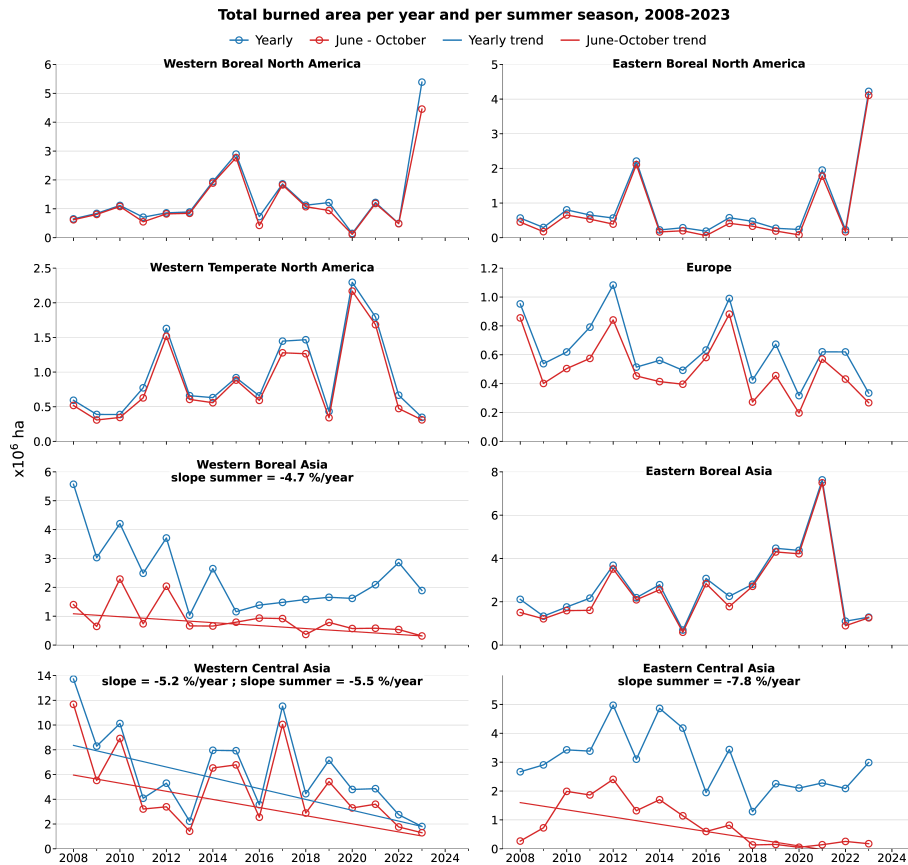
**Figure 3.** Total yearly burned area and June–October burned area from 2008 to 2023 in regions of Fig. 1, and corresponding linear regression. Only regions with a significant trend either for total yearly burned area or total June–October burned area (p<0.1) are provided. Note the different y-axis limits between panels.

As presented in Fig. 3, a negative trend is obtained in regions where the burning is primarily associated with agricultural practices. In Western Central Asia, a significant decrease in both the total yearly and June-October burned area of about -5 %.year[-1] is obtained. However, in Eastern Central Asia and Western Boreal Asia, a significant decrease is obtained only during June-October (-7.8 %.year[-1] and -4.7 %.year[-1], respectively). In Europe and Eastern Boreal North America, while decreasing trends may be obtained for specific months (-4 %.year[-1] in August in Europe and -5 %.year[-1] in October in Eastern Boreal North America), no significant trend is obtained over the full year or season.

No upward monthly or seasonal trend is observed in the selected regions. However, an upward trend of +101 %.year[-1] is observed in September in Western Temperate North America. It is crucial to acknowledge the considerable interannual variability, particularly when considering the limited number of years included in the study period (2008–2023). For example, when the year 2023 is excluded, an increasing trend in the annual regional burned area of approximately +18 %.year[-1] is

**Table 1.** Trends during the 2008–2023 period and evolution during recent years for key variables of fire activity and fire weather during June–October, over selected regions of the Northern Hemisphere. The recent evolution of a given variable $X$ is calculated as the difference between the values averaged over the 2017–2023 period (recent period) minus values averaged over the 2008–2023 period (full period), so that the relative difference is defined as $(\overline{X_{recent}} - \overline{X_{full}})/\overline{X_{full}}$. The symbol * indicates that the trends or the absolute difference $(\overline{X_{recent}} - \overline{X_{full}})$ is significant (p-value<0.1)

| Variable ($X$) | West. Boreal North America | East. Boreal North America | West. Temperate North America | Europe | East. Boreal Asia | East. Central Asia |
|---|---|---|---|---|---|---|
| **Burned area (BA), regional June–October total** | | | | | | |
| Mean 2008–2023 ($10^6$ ha) | 1.2 | 0.7 | 0.8 | 0.5 | 2.5 | 0.8 |
| Trend 2008–2023 (%.year$^{-1}$) | 4.4 | -1.5 | 6.9 | -3.1 | 15.8 | -7.8* |
| Difference recent vs full period (%) | 15.8 | 36.9 | 27.6 | -13.2 | 28.9 | -71.3* |
| **Fire radiative power ($FRP$), regional June–October average** | | | | | | |
| Mean 2008–2023 ($MW$) | 113 | 40 | 212 | 41 | 82 | 9 |
| Trend 2008–2023 (%.year$^{-1}$) | 1.4 | 0 | 2.6 | 4.1* | 0.1 | 3.0 |
| Difference recent vs full period (%) | 10.8 | 1.4 | 8.1 | 18.0 | 3.2 | 19.0 |
| **Fire Weather Index ($FWI$), regional June–October average** | | | | | | |
| Mean 2008–2023 | 3.9 | 3.2 | 31.7 | 8.1 | 3.8 | 13.8 |
| Trend 2008–2023 (%.year$^{-1}$) | 0.7 | 2.9* | -0.1 | 0.5* | 2.4 | -0.5 |
| Difference recent vs full period (%) | 2.2 | 11.1 | 0.4 | 2.7 | 7.2 | -1.1 |
| **Fire Weather Index ($FWI$) 97th percentile, regional June–October average** | | | | | | |
| Mean 2008–2023 | 16.2 | 14.9 | 64.3 | 18.9 | 17.9 | 36.0 |
| Trend 2008–2023 (%.year$^{-1}$) | 0.6 | 3.0* | -0.1 | 0.1 | 1.0* | -0.1 |
| Difference recent vs full period (%) | -0.7 | -0.4* | -0.2 | 3.4 | 2.7 | 0.6 |

observed in Western Temperate North America and Eastern Boreal Asia. This is particularly pronounced during the months of June to October, with an increase of +23% and +25 %.year$^{-1}$ during the period 2008–2022.

Our results align with the review conducted by Jones et al. (2022). In order to facilitate quantitative comparisons, the indicator employed in the review is calculated for the period spanning from 2008 to 2023. Table A1 presents a comparison between the results of our study and those of the review by Jones et al. (2022). Both estimates indicate a relative increase in the annual burned area in Western Boreal and Temperate North America, as well as in Eastern Boreal Asia and more widely across all boreal and temperate North America. Additionally, both studies indicate a relative decrease in annual regional burned area in Europe and Central Asia. This reduction may be attributed to a decline in agricultural burning.

260

## 3.3 Anomalies in fire activity during recent years

Although no significant positive trends in regional burned area were obtained for the 2008-2023 period, some regions have experienced particularly large burning seasons in the recent years (boreal regions, Western Temperate North America), as shown in Figure A1. To characterise this evolution, the difference in fire activity between the period 2017–2023 and the full time period (2008–2023) is calculated, focusing on the months June to October.

Figure 2 (f) shows the relative difference in seasonal burned area. In regions identified as affected by land management and agricultural fires (high burned area, high frequency), seasonal burned area in recent years is lower than the average over the full period (regionally averaged relative difference equal to -34 %, -17 % and -13 % for Western Boreal Asia, Western Central Asia, and Eastern Temperate North America, respectively), which is consistent with the significant negative trends obtained. Regions identified as affected by intense wildfires (Eastern Boreal Asia, Western Boreal and Temperate North America), exhibited a more pronounced increase in seasonal burned area than the rest of the Northern Hemisphere (average regional values in Table 1).

The evolution of key fire characteristics at regional scale is shown in Fig. 4. These key variables are the total burned area, the number of fire events with average fire radiative power $\leq 500\,\mathrm{MW}$ (low or moderate fire intensity) and the number of fire events with average FRP $> 500\,\mathrm{MW}$ (intense events). Since fire characteristics may evolve as the fire season progresses, the relative difference between recent years (2017–2023) and the full period (2008–2023) is calculated for each variable considering either the full season (June–October), the early season (June–July), the middle season (July–August) or the late season (September–October). Using the same approach, the evolution of the total number of events, the average burned area per event and the average length of events is shown in Fig. A2, and the evolution depending on the average burned area per event is shown in Fig. A3.

The regions identified as affected by intense fires, namely Western and Eastern Boreal North America, Western Temperate North America and Eastern Boreal Asia, have experienced higher regional June–October burned area during recent years (+16 %, +37 %, +28 % and +29 % respectively). The number of events has increased in all regions but also their length (and thus the mean burned area per event) and the number of intense events. This suggests an increase in intense fire events in these regions.

In Western Temperate North America and Eastern Boreal Asia, the regional burned area is higher during recent years during all periods of the fire season. In North America (boreal and temperate), the increase is particularly marked towards the end of the fire season and for events with burned area $> 1\,000$ hectares (ha). This is attributable to both a greater average number of fire events and longer, more intense, events. In Eastern Boreal North America, the decrease in burned area towards the end of the season appears to be attributed to a reduction in low-intensity events, which was partially compensated by an increase in intense events.

In Europe, the situation is contrasted. The average burned area and the number of events are both lower in recent years. This decline is observed across all fire radiative power classes, with the exception of intense events during the early and middle season (+40 % for June–July and +46 % for July–August). Events with a total burned area exceeding 1 000 ha exhibit a
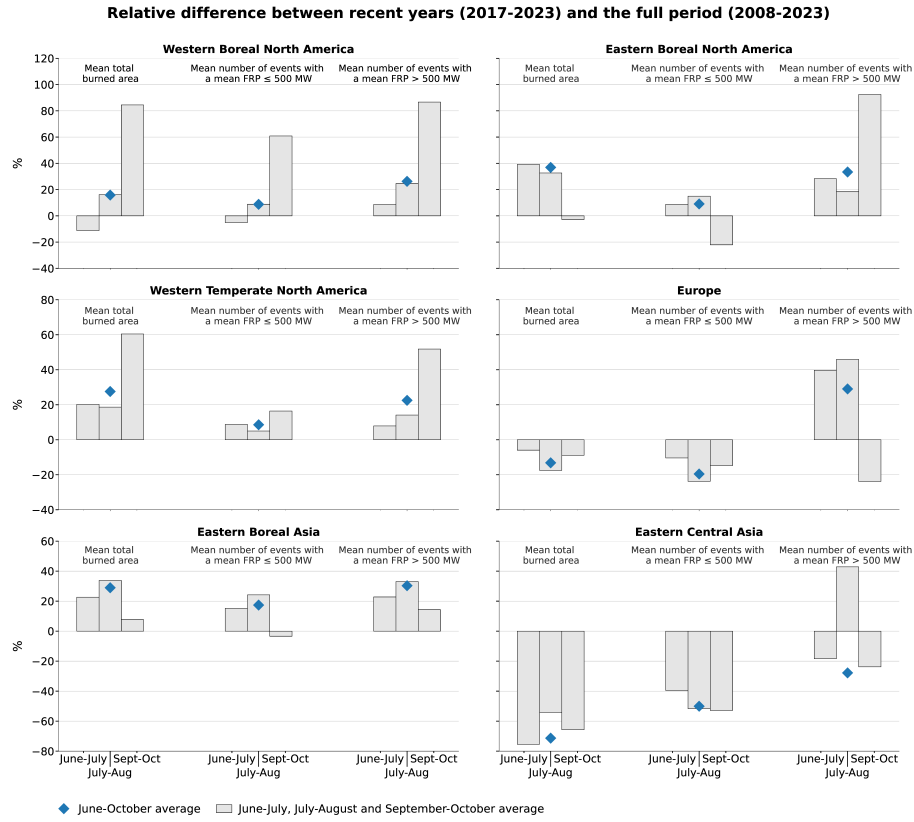
**Figure 4.** Relative difference between recent years (2017–2023) and the full period (2008–2023) of different fire characteristics and the regions mapped in Fig. 1 during time periods June–October, June–July, July–August or September–October: average total burned area, average number of fire events with an average fire radiative power (FRP) $\leq 500\,\mathrm{MW}$, average number of fire events with an average fire radiative power (FRP) $> 500\,\mathrm{MW}$. The difference is calculated as (recent-full)/full. The June–October average relative differences, represented here as the blue diamonds, are the difference values presented in Table 1

comparatively lower decrease, and even an increase during June-July. The mean burned area per event and the duration of fire
300 events are also higher, particularly in the late season (respectively +120 % and +9 % for September–October). This indicates an
increase in intense wildfires despite a general decrease in the number of fires.

In Eastern Central Asia, a region characterised by agricultural fires, the average burned area and the number of fire events
are both lower across all periods. A significant decrease (-50 % to -100 %) in burned area during June–July is observed in the
North China Plain, where farmers burn wheat stubble to fertilise the soil (Hall et al., 2024). Similarly, significant decreases are
305 observed in the northeastern part of China towards the end of the fire season. This coincides with corn harvesting, which is
extensively cultivated in this region. Since 2018, the extent of burned area in the region during the summer months has been
minimal (Fig. A1). Nevertheless, the total burned area in the region increases in April, with a positive trend of +40 %.year$^{-1}$.
Despite the implementation of policies aimed at regulating agricultural fires in China, the practice of straw burning persists
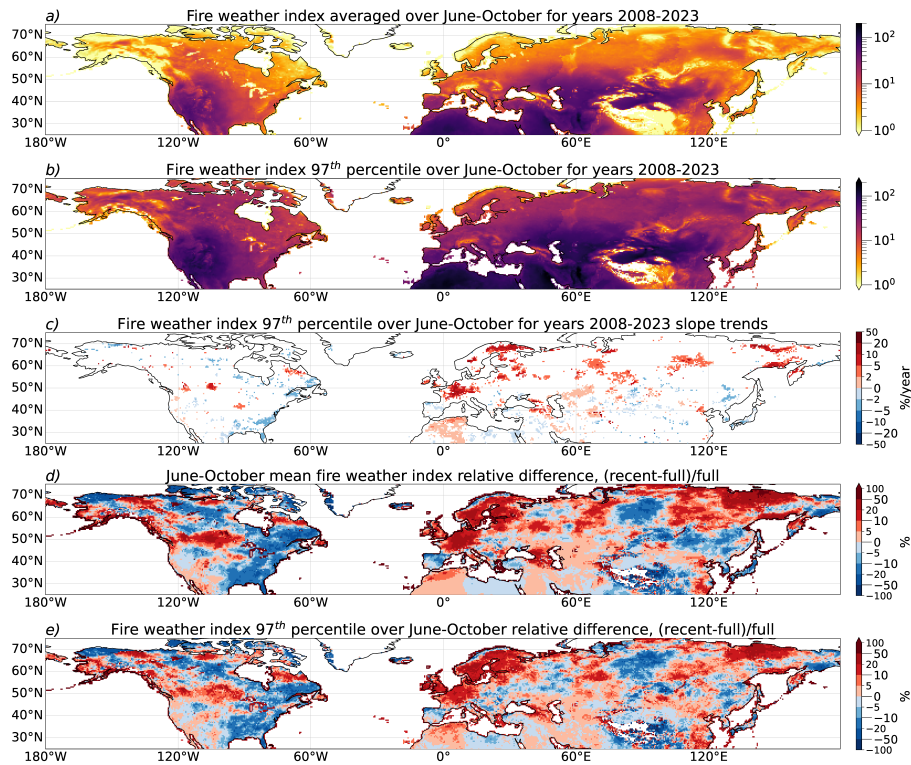
**Figure 5.** (a) Fire weather index averaged over June–October for years 2008–2023, (b) associated 97th percentile, (c) trends in fire weather index 97th percentile (only significant trends are plotted, with p value < 0.1), (d) difference between average fire weather index for 2017–2023 compared to 2008–2023, (e) difference between fire weather index 97th percentile for 2017–2023 compared to 2008–2023. Differences are calculated as (recent-full)/full.

in agricultural regions. This is particularly prevalent in north-eastern China, which accounted for 56 % of agricultural fires
310  detected in China between 2014 and 2018 (Wang et al., 2023). The observed evolution is consistent with the findings of
Zhuang et al. (2018), who demonstrated that the number of fires in spring has consistently increased between 2003 and 2017 in
north-eastern China, while the number of fires in summer has significantly declined between 2012 and 2017 in eastern China.

### 3.4 Fire weather index evolution

The evolution of the Fire Weather Index (FWI) is analyzed to verify whether changes in meteorological conditions over the
315  study period can explain the observed evolution of fire activity. The horizontal distribution of the FWI averaged over the June–
October 2008–2023 period, and of the extreme FWI (defined as the 97th percentile of the seasonal distribution in each grid
cell) over the same period, are shown in Fig. 5 (a) and (b). Trends over the period 2008–2023 and relative differences between
recent years (2017–2023) and the whole period are also shown for the extreme seasonal FWI (similar structures are obtained
for the average FWI) in Fig. 5 (c), (d) and (e). Regional averages over selected regions of interest are provided in Table 1,

with the associated trends and anomalies. Anomalies for June–July, July–August and September–October periods are details in Table A2.

Both the mean FWI and the 97$^{th}$ percentile of its distribution are larger at latitudes below $\sim 50\,°N$ (FWI $\gtrsim 10$) than at higher latitudes. The trends and recent anomalies show consistent patterns, although significant trends are limited to relatively small regions.

Significant positive trends are obtained in Europe (more specifically in northern Europe) and Eastern Boreal Asia (Fig. 5 (c)). In Eastern Boreal Asia, a significant positive trend of +1.0 %.year$^{-1}$ is obtained for the regionally averaged extreme FWI. The seasonal anomaly is higher at the end of the season (+3.6 %) for the extreme FWI, while it is higher at the beginning of the season for the average FWI (+6.7 %). The observed change in the average FWI aligns with the increase in fire activity during recent years. However, it does not align with the intra-seasonal variation in fire activity (maximum increase in observed burned area during July–August).

In Eastern Boreal North America, a significant positive trend is obtained for the regional average June–October FWI (+2.9 %.year$^{-1}$) and the extreme June–October FWI (+3.0 %.year$^{-1}$). The seasonal extreme FWI is lower during recent years across all periods. The greatest decrease occurred towards the end of the season, with a reduction of -4.9 %. Conversely, the average value is higher during recent years, particularly towards the end of the season (+14 %). The recent increase in fire activity and intensity during the late season may be attributed to the increase in weather conditions favorable to fire spread.

No significant trend is obtained for the regional averages of the FWI and extreme FWI in western boreal and western temperate North America, and the average FWI in recent years is only slightly higher than the average over the full period. The extreme FWI is on average lower in recent years in these regions. However, there are strong horizontal gradients, and the maps show strong increases in some areas that are experiencing a sharp rise in fire activity (e.g. western Canada, Pacific Northwest) (Fig. 5 (d) and (e)). Compared with the full June–October period, the extremes and anomalies of recent years are higher at the end of the season for both regions (not shown). The observed increase in fire risk in recent years, particularly towards the end of the season, is consistent with the observed increase in fire activity and intensity.

According to the evolution of the FWI, fire risk decreased in eastern North America, which explains the absence of a significant trend in fire activity in this region. In eastern Europe, Ukraine and Western Central Asia, no clear downward trend or negative anomaly in FWI is obtained, suggesting that the observed decline in fire activity is more likely attributable to human intervention than to a change in fire risk.

## 4 Results on variability and trends in CO and AOD

### 4.1 Variability of CO and AOD during 2008–2023

The horizontal distribution of average and extreme total columns of CO (designated as CO) and AOD during June–October 2008–2023 are shown on Fig. 6. Extreme values are defined as the 97$^{th}$ percentile of the distributions of CO and AOD in each grid cell.
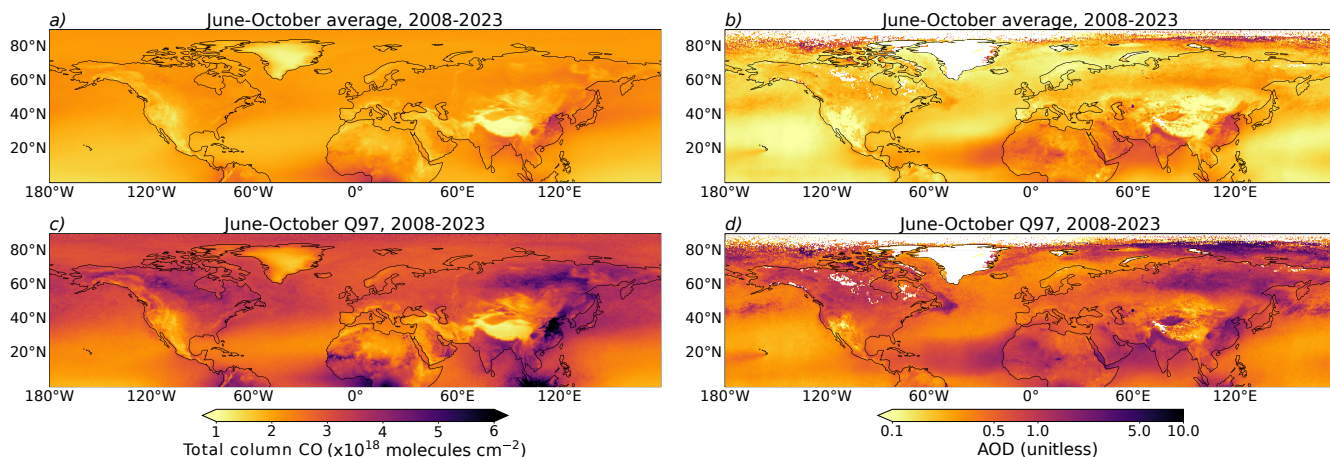
**Figure 6.** Left panels: total column CO observed by the IASI instrument, averaged on a 0.5°×0.5° grid for June–October 2008–2023 (top), as well as the 97th percentile of the distributions during June–October (bottom). Right panels: Same for the AOD observed by the MODIS instrument.

The lowest CO is observed above high altitude surfaces and reliefs, while the highest CO is observed over southern and eastern Asia, and Africa (at the limit of the domain). Relatively large background CO values are due to secondary production (oxidation of methane and volatile organic compounds) as well as long-range transport. Transported plumes are smoothed by the averaging but the influence of long-range transport is still discernible over the Pacific and Atlantic Oceans. Larger spatial variability is obtained for the extreme CO. Particularly high values are observed above Siberia, Western Boreal North America and much of the western United States. As shown in the previous section, these regions correspond to areas prone to intense fire activity in the summer (see Fig. 2). Extreme CO is also elevated over the northern Pacific and Atlantic, highlighting the transport of CO plumes resulting from extreme fires in North America and Siberia.

Despite substantial fire activity, Western Central Asia does not exhibit a level of extreme CO values comparable to those observed in the aforementioned regions. This is likely attributable to a combination of factors, including lower emissions and a reduced influence from long-range transport. This suggests that fires in Western Central Asia, although frequent, are less intense and emit less CO than the extreme fires in boreal regions or the western United States. This may also partly reflect CO concentrations that remain at low altitude (boundary layer), where the sensitivity of the IASI instrument decreases (Clerbaux et al., 2009). Over Southern and Eastern Central Asia, large extreme CO is observed despite low fire activity, probably due to the impact of anthropogenic emissions (Boynard et al., 2014). Zheng et al. (2019) estimate that biomass burning emissions of CO in China in 2000–2017 represent only about 2 % of anthropogenic emissions. In contrast, they estimate that biomass burning emissions are 50 % larger than anthropogenic emissions in Canada.

Similar features are observed for AOD (Fig. 6 (b) and (d)), but with lower background values than for CO due to shorter lifetimes. It is worth noting that high AOD values are also observed over the Middle East, North Africa and the southern part

of the North Atlantic ($\sim 20\,°N$) due to dust emissions and transport. A simultaneous increase in AOD and CO can be used to distinguish the signature of combustion plumes from that of dust transport.

Both CO and AOD are characterised by marked seasonal cycles. For CO, it is strongly linked to the CO lifetime with respect to oxidation by OH, that is maximum during winter (minimum OH) and minimum during summer (e.g. Edwards et al., 2004; Buchholz et al., 2021). The accumulation of CO during winter explains the maximum CO observed in spring in most regions. Similarly, higher reactivity during summer leads to minimum CO in September–October. The temporal variations are also influenced by the seasonal variations in emissions (both anthropogenic and biomass burning) and the associated transport pathways.

The variability of AOD in each region is greater than that of CO. Aerosols having a shorter lifetime than CO, their background concentration is also lower so that the spatial variability in AOD is strongly impacted by the horizontal and temporal variability of regional sources (anthropogenic emissions, dust uplift, fires, marine sources, and secondary production). A maximum in AOD from April to August and a minimum in December in most regions are observed (Edwards et al., 2004; Buchholz et al., 2021).

The correlation coefficient between the June–October and the July–August annual regional average CO and AOD is calculated (Table A3). A strong correlation ($r > 0.7$) is found for the July–August period in Western North America and Eastern Boreal Asia, which is consistent with fire activity in these regions leading to peaks in AOD and CO. In some regions, CO peaks are observed without an associated AOD peak which illustrates the longer-range transport of CO. However, large CO and AOD plumes can be transported simultaneously at intercontinental scale in the case of large wildfires, as suggested by the significant correlations obtained above the Atlantic Ocean, and as further discussed in section 4.4.

The link between fire activity and the observed variations of CO and AOD is analyzed using the Pearson correlation coefficients between the June–October burned area for latitudes greater than $30\,°N$, excluding the agricultural regions of Western Asia (Western Boreal and Western Central Asia), and CO (Table A3).

For average CO observed in June–October, the correlation coefficient is larger than $\sim 0.7$ for all regions, which confirms that biomass burning is a strong driver of temporal variability. A significant correlation (p-value < 0.1) between the average CO observed in June–October and in December is also obtained in Western and Eastern Boreal North America and Eastern Central Asia. The correlation coefficient is also significant between the average CO in December and the June–October regional burned area during the previous years for all regions (Table A3). This reflects the accumulation of CO due to summer emissions from biomass burning, in agreement with previous studies (Edwards et al., 2004). Although focusing on the June–October period allows us to analyze the temporal evolution of CO and AOD, when the relative contribution of forest fires is at its maximum, intense forest fires will not only have an impact on CO concentrations during the summer, but also during the autumn and winter that follow.

## 4.2  Trends in CO and AOD during 2008–2023

Figure 7 shows the horizontal distribution of the 2008–2023 trends of the June–October average CO and extreme CO (97th percentile). The regional mean of significant trends is shown for each study region, and summarised in Table 2.
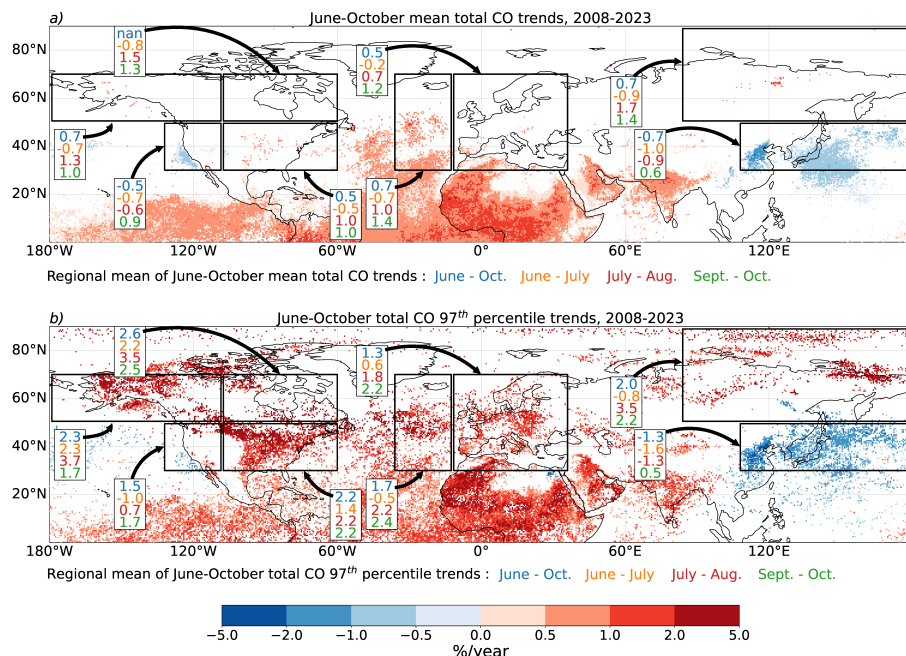
**Figure 7.** Trends in IASI CO during 2008–2023 for (a) the June–October mean CO, and (b) the June–October 97th percentile of CO. Only significant trends (p < 0.1) are shown. "nan" in (a) indicates that no significant trend is observed in the study region.

While past studies show that the annual CO in the Northern Hemisphere decreases due to decreasing anthropogenic emissions (Zheng et al., 2018; Buchholz et al., 2021), we find that, when focusing solely on the months of June to October, the extent of the significant downward trends is relatively limited and is concentrated in regions of Eastern Central Asia, the northern Pacific Ocean and western Temperate North America (Fig. 7 (a)). Positive mean trends of +0.5 to +0.7 %.year$^{-1}$ are obtained for Western Boreal North America, Eastern Boreal Asia, the Atlantic and Europe, although with a relatively small number of significant trends.

June–October extreme CO show more pronounced trends (Fig. 7 (b)). The observed changes are significant and positive over the majority of the Northern Hemisphere (+1.3 to +2.6 %.year$^{-1}$ in North America, Europe and Eastern Boreal Asia), with the exception of Asia and the northern Pacific (1.3 %.year$^{-1}$ in eastern Asia). Trends increase as the season progresses and, while some trends are negative in June–July in several regions, they are all positive at the end of the season (September–October). This indicates an increase in emissions, long-range transport and a buildup of CO over the summer. The regions exhibiting the most pronounced positive trends correspond to those experiencing increasingly severe fire seasons in recent years, namely Eastern Boreal Asia and Western Boreal North America (see sect.3.2-3.4). However, it is also notable that regions situated downwind of these areas (eastern North America, the Atlantic, Europe) also demonstrate a positive trend.

Using satellite observations of CO from another instrument (MOPITT/TERRA), Buchholz et al. (2022) also found an increase in CO over North America for the period 2002–2018 in August (significant positive trends at gridcell scale up to

**Table 2.** Trends and evolution during recent years for key variables $X$ of total column CO and AOD during June–October. The recent evolution of a given variable $X$ is calculated as the difference between the values averaged over the 2017–2023 period (recent period) minus values averaged over the 2008–2023 period (full period), so that the relative difference is defined as $(\overline{X_{recent}} - \overline{X_{full}})/\overline{X_{full}}$. Mean trend* $X$ corresponds to the regional mean of significant trends at the grid cell scale. The symbol * indicates that the trends or the absolute difference $(\overline{X_{recent}} - \overline{X_{full}})$ is significant (p-value<0.1).

| Variable ($X$) | West. Boreal North America | East. Boreal North America | West. Temperate North America | Atlantic | Europe | East. Boreal Asia | East. Central Asia |
|---|---|---|---|---|---|---|---|
| **total column CO, June–October regional average** | | | | | | | |
| Mean 2008–2023 ($\times 10^{18}$ molecules.cm$^{-2}$) | 2.1 | 2.1 | 1.8 | 2.0 | 2.0 | 2.2 | 2.4 |
| Trend 2008–2023 (%.year$^{-1}$) | 0.1 | 0.2 | 0.1 | 0.5 | 0.2 | 0.1 | -0.4* |
| Mean trend* 2008–2023 (%.year$^{-1}$) | 0.7 | – | -0.5 | 0.7 | 0.5 | 0.7 | -0.7 |
| Difference recent vs full period (%) | 1.1 | 1.3 | 0 | 2.6 | 1.6 | 0.8 | -2.7 |
| **total column CO 97th percentile, June–October regional average** | | | | | | | |
| Mean 2008–2023 ($\times 10^{18}$ molecules.cm$^{-2}$) | 3.4 | 3.5 | 2.6 | 3.0 | 2.7 | 3.5 | 3.7 |
| Trend 2008–2023 (%.year$^{-1}$) | 1.0 | 2.0 | 0.1 | 0.8 | 0.5 | 0.4 | -0.96* |
| Mean trend* 2008–2023 (%.year$^{-1}$) | 2.3 | 2.6 | 1.5 | 1.7 | 1.3 | 2.0 | -1.3 |
| Difference recent vs full period (%) | 8.0 | 9.3 | 5.8 | 7.3 | 5.4 | 3.0 | -4.9 |
| **AOD, June–October regional average** | | | | | | | |
| Mean 2008–2023 | 0.2 | 0.2 | 0.1 | 0.1 | 0.2 | 0.3 | 0.2 |
| Trend 2008–2023 (%.year$^{-1}$) | 2.4* | 2.7 | 2.0 | 1.1 | -0.5 | 0.6 | -2.1* |
| Mean trend* 2008–2023 (%.year$^{-1}$) | 7.6 | 6.9 | 4.1 | 2.4 | -1.1 | 8.5 | -2.4 |
| Difference recent vs full period (%) | 13 | 9.2 | 15 | 7.1 | -0.6 | 27 | -12* |
| **AOD 97th percentile, June–October regional average** | | | | | | | |
| Mean 2008–2023 | 0.7 | 0.7 | 0.5 | 0.4 | 0.5 | 1.2 | 0.7 |
| Trend 2008–2023 (%.year$^{-1}$) | 7.8* | 11.3 | 7.1 | 2.2* | 0.0 | 2.8 | -3.2* |
| Mean trend* 2008–2023 (%.year$^{-1}$) | 36 | 17 | 15 | 4.5 | 1.7 | 223 | -2.6 |
| Difference recent vs full period (%) | 22 | 10 | 33 | 13 | -0.9 | 16 | -15* |

+1.5 %.year$^{-1}$ in the Pacific Northwest), while concentrations tend to decrease during other months. Our study confirms increasing trends during 2008–2023 over this region, and demonstrates that wildfires in Eastern Boreal Asia and Western Boreal and Temperate North America may also affect trends in the Atlantic and Europe throughout the fire season, and not only in August. Indeed, positive trends in regional average CO are observed in the Atlantic in August (+1.2 %.year$^{-1}$), in
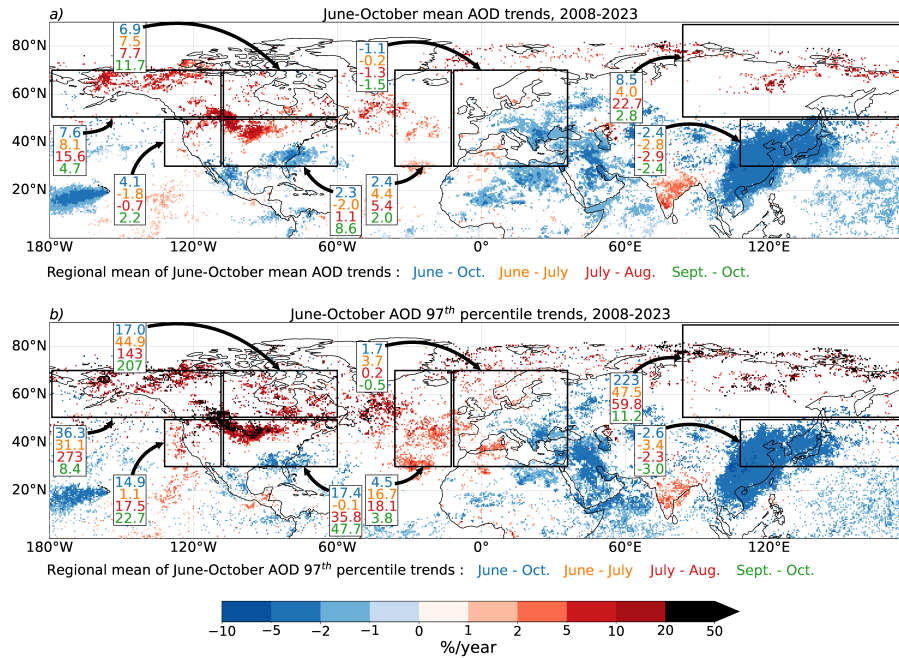
**Figure 8.** Same as Fig. 7 but for the AOD observed by the MODIS instrument.

September (+1.8 %.year⁻¹) and in October (+0.98 %.year⁻¹) as well as in Europe in September (+1.4 %.year⁻¹) and in October (+0.7 %.year⁻¹).

Figure 8 illustrates the significant trends in AOD. The horizontal structures observed in the June-October average and the June-October extremes are comparable. Negative trends are observed in Eastern Central Asia and the Pacific Ocean for both the average and the extreme AOD, in agreement with the results obtained for CO. In the boreal regions, the regional mean trends in June–October AOD are positive regardless of the studied period (+7.6 %.year⁻¹ in Western Boreal North America, +8.5 %.year⁻¹ in Eastern Boreal Asia). It can be observed that regions affected by intense wildfires exhibit strong and significant positive trends, with larger trends for extreme AOD than for the average AOD. The average increase in extreme AOD over the entire fire season is +36.3 %.year⁻¹ for Western Boreal North America and +223 %.year⁻¹ for Eastern Boreal Asia.

In Western Temperate North America, the average trend is negative at the beginning of the season (-1.8 %.year⁻¹) and in the mid-season (-0.7 %.year⁻¹), and positive at the end of the season and on average over June-October (+4.1 %.year⁻¹) (Fig. 8 (a)). This is consistent with the findings of Buchholz et al. (2022), who find a trend of +8 %.year⁻¹ in AOD in the Pacific Northwest for the period 2002-2018. With regard to extreme values, the greatest increase is observed during the mid-season, with an annual increase of +273 %.year⁻¹ (Fig. 8 (b)).

Over the Atlantic, the regional mean of significant trends is positive for all periods, with an increase of 5.4 %.year⁻¹ for mean June–October AOD and 18.1 %.year⁻¹ for June–October extreme values. The highest increase is observed during the mid-season.
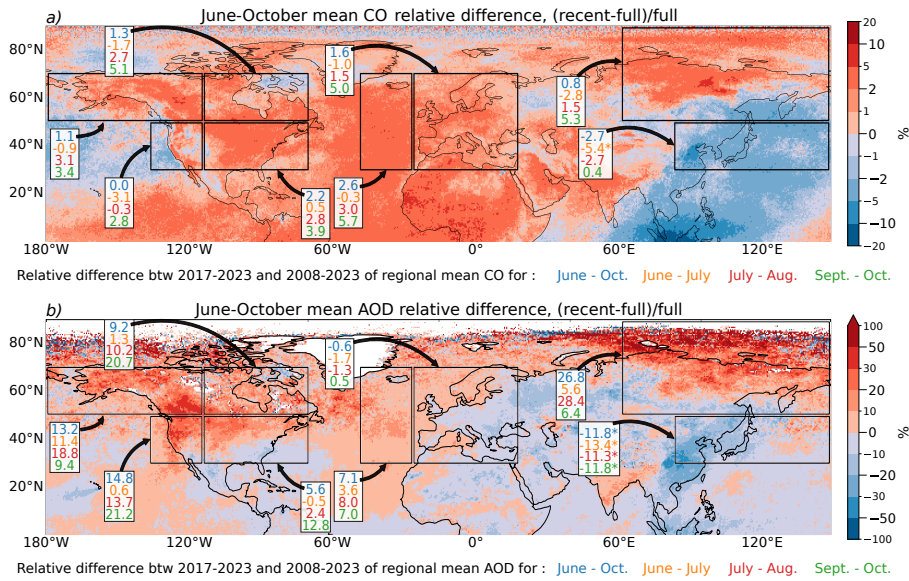
**Figure 9.** Relative difference between June–October (a) average CO during recent years (2017–2023) and the full period (2008–2023) and (b) average AOD during recent years (2017–2023) and the full period (2008–2023). The symbol * indicates that the absolute difference $(\overline{X_{recent}} - \overline{X_{full}})$ is significant (p-value<0.1)

In Europe and Eastern Central Asia, a negative trend is observed for the June–October mean AOD. A minimum is observed in Europe at the end of the season, with a decrease of -1.5 %.year$^{-1}$, while a minimum is observed in Eastern Central Asia in the mid-season, with a decrease of -2.9 %.year$^{-1}$ (Fig. 8 (a)). In Western Europe, there is a significant positive trend in extreme
445 values (Fig. 8 (b)). This indicates that the impact of strong local emissions and of the long-range transport of wildfire plumes over the Atlantic Ocean is increasing, offsetting the otherwise negative trends in AOD.

In regions prone to intense wildfires, the impact of wildfires on local AOD is greater than that of CO, due to the shorter lifetime of aerosols. However, our study shows that the Atlantic and western Europe are also significantly affected by an increase in AOD. The significant impact of wildfires on extreme values demonstrates that large-scale wildfire events can offset
450 a general decline in AOD throughout the year.

At lower latitudes, a considerable positive trend is discernible for both CO and AOD over India, mostly located over the continent for AOD. Positive trend in CO are also observed over Africa and the tropical Atlantic Ocean, but they are not accompanied by a positive trend in AOD. This discrepancy may be attributed to a lower contribution of combustion to AOD in this region, in comparison to the substantial influence of mineral dust. These features warrant further investigation, although
455 this is beyond the scope of this study, which primarily aims to understand the evolution in extratropical regions of the Northern Hemisphere during summer.

## 4.3 Anomalies in CO and AOD during recent years

As shown in Section 3, the analysis of burned area does not show significant increasing trends in the regions considered, but the anomalies during recent years (2017–2023) compared to the whole period (2008–2023) are strongly positive in Eastern Boreal Asia and Western North America. Using the same approach, relative differences for the mean June–October CO and AOD are shown in Fig. 9. Regional mean anomalies are also indicated (summarised in Table 2 for some key regions).

The structures are consistently aligned with the significant trends observed from June to October (Fig. 7 and 8), which confirms the results obtained in the previous section on areas rather limited by the trend significance test. Regions with significant negative trends show a negative anomaly during recent 7 years (Eastern Central Asia and the northern Pacific, -2.7 % for CO and -11.8 % for AOD), and regions with significant positive trends show a positive anomaly in recent years (further discussed below). Anomalies and trends are both larger for AOD than for CO, except above Europe.

Regions that have experienced more wildfires in recent years show positive anomalies. All regions experience lower average anomaly in CO at the beginning of the season, and larger average anomaly in CO at the end of the season, again showing the accumulation as the fire season progresses (Fig. 9 (a)).

In this subsection, the results are examined region by region in relation to the evolution of fire activity, although a given region is not only influenced by regional biomass burning emissions but by a combination of various local emission sources, chemical evolution and long-range transport. The total hemispheric burned area will be used to study the evolution of the number of plumes of extreme values in section 4.4.

Eastern Boreal Asia encompasses areas with positive and negative anomalies for both CO and AOD. Negative anomalies are linked to the decreasing Asian outflow. However, the average anomalies remain positive: +0.8 % for June–October CO, increasing during the season to +5.3 % in September–October, and +26.8 % for AOD, with a maximum in July to August. Analysis of fire activity (section 3, Table 1) indicates that, in this region, the burned area for the period June to October has increased in recent years by +29 %, with an increase in the number of events, their duration and their intensity, accompanied by an increase in the extreme values of fire risk. The regional burned area anomaly in Eastern Boreal Asia is largest during mid-season, in agreement with a particularly large increase in AOD. Within the region, the maximum anomalies are obtained above eastern Siberia, in agreement with a large increase over this region for burned area (Table A1), and extends towards the Arctic. However, the observations at high latitudes ($> 70\,°N$) are more noisy and may be less reliable (especially for AOD).

In Western and Eastern Boreal North America, positive anomalies are observed for both the June–October average CO ($\sim$ +1 %) and AOD (+13.2 % in Western and +9.2 % in Eastern Boreal North America). For CO, the anomaly is negative in June–July but positive later in the season, with a maximum in September–October (+3.4 % and +5.1 % for Western and Eastern Boreal North America, respectively). The anomaly in AOD is positive during the whole summer, and maximum in July–August in Western Boreal North America and in September–October in Eastern Boreal North America. These results are consistent with the evolution of fire activity, which showed an increase in fire risk, in burned area (+16 % in Western and +37 % in Eastern Boreal North America for June–October), and in intense events, particularly at the end of the fire season (+87 % in Western and +92 % in Eastern Boreal North America for events with a mean fire radiative power $> 500\,MW$ for September–October).

In Eastern Boreal North America, it seems that the increase in intense events towards the end of the season and transport from the west have a greater impact on AOD and CO than the decline in total regional burned area (-3 % in September–October).

In Western Temperate North America, the average CO has remained relatively stable during the fire season, due to lower concentrations in the Pacific and larger concentrations in coastal areas (Fig. 9 (a)). The anomaly is negative in the months of June to August, but positive in the months of September to October (+2.8 %). The regional AOD, less influenced by long range transport, shows a positive anomaly (+14.8 % from June to October), with a peak at +21.2 % at the end of the season (Fig. 9 (b)). It is also possible to relate these results to the occurrence of strong positive anomalies in fire activity (+28 % increase in the regional burned area, increase in fire intensity and event length) and fire risk (+2 % increase in extreme fire weather index), which are particularly large at the end of the season.

For both CO and AOD, the positive anomalies extend downwind, encompassing the eastern United States, the northern Atlantic, and western Europe in particular.

Eastern Temperate North America was not identified as a region with increasing fire activity. Nevertheless, both the observed trends and the recent anomalies are positive for CO and AOD, particularly over the northern half of the region. A consistent increase in CO and AOD over this region was also obtained at different periods by Buchholz et al. (2022) and linked to an increasing influence of long-range transport from fire plumes.

Both CO and AOD anomalies are positive above the northern Atlantic region, with a maximum in September–October for CO (+5.7 %) and in July–August for AOD (+8 %). The regional AOD anomaly above the Atlantic peaks at the same time as the regional AOD anomaly and fire activity above Western Temperate North America. Above Europe, the regional CO anomaly is positive over most of the region (+1.6 %), although there are negative anomalies during June–July. In contrast, the regional AOD anomaly is positive only over parts of western, northern Europe and the Mediterranean, which is consistent with the significant trends. The anomalies exhibit an increase during the summer months, reaching their maximum in June–October (+5 % and +0.5 % for regional CO and AOD anomalies, respectively). This indicates an increase in the influence of long-range transport of wildfire plumes during the summer, which compensates for an otherwise negative anomaly.

### 4.4 Plumes of extreme CO and AOD and link with wildfires

The evolution of extreme concentrations of CO and aerosols is further analysed in terms of the number of days affected by extreme pollution plumes during June–October. A pollution plume is identified using the extreme values in either CO alone or CO and AOD combined, as detailed in section 2.5. The latter will be indicative of fresher plumes, and allows the identification of aerosol plumes that are linked to a strong combustion source. Figure 10 illustrates the number of days from June to October in which a CO plume is detected, as well as instances where both CO and aerosol plumes are simultaneously present in each region of interest. The mean values for the full 2008–2023 period, as well as the recent anomalies, are presented in Table 3.

As anticipated, the number of days affected by extreme plumes of CO and AOD combined is lower than the number of days affected by extreme plumes of CO alone. The difference is particularly large above regions that are predominantly influenced by long-range transport (the Atlantic and Europe). Furthermore, a significant interannual variability is observed, which may be linked to the variability in fire activity.
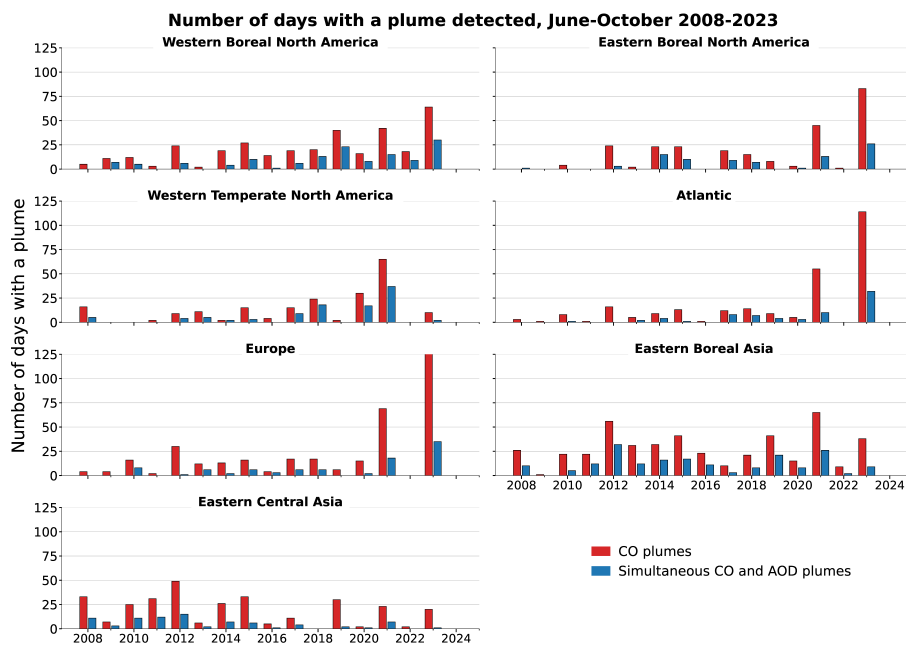
**Figure 10.** Number of days with a plume detected during June-October 2008-2023. The data bars in red correspond to the number of days from June to October with CO plumes, while the data bars in blue correspond to the number of days from June to October with simultaneous CO and aerosol detected plumes.

Table A3 presents the Pearson correlation coefficient between the monthly number of days with a detected CO plume and the burned area in various regions. burned area in Eastern Boreal Asia are positively correlated with plumes in Eastern Boreal Asia and Western Boreal and Temperate North America. The number of days with a detected plume in Eastern Boreal Asia, Western Boreal and Temperate North America, the Atlantic and Europe is positively correlated ($r > 0.5$) with burned area in Western Temperate North America. The impact of fires on the number of plumes in the Eastern Central Asia region appears to be minimal. The total monthly burned area in all grid cells located above 30 °N shows a correlation above 0.5 with plumes in regions Eastern Boreal Asia and Western temperate North America. If burned area is calculated without the contribution from Western Central Asia and Western Boreal Asia, where the burning is mainly linked to agricultural practices, the correlation increases across all regions. This indicates that agricultural burning contributes less to the CO observed by IASI in the Northern Hemisphere than wildfires. As previously stated, this may be attributed to a combination of lower emissions and a lower altitude of the resulting plumes.

Figure 11 illustrates the cumulative number of days with CO plumes (i.e., the sum of days with a detected plume in each of the following region: Western and Eastern Boreal North America, Western Temperate North America, the Atlantic, Europe, Eastern Boreal and Eastern Central Asia) and the total burned area for June–October of every year in the study period (2008–2023). The total burned area is calculated for the latitude range above 30 °N, excluding the Western Central and Western Boreal Asia regions. The figure also depicts the relative contribution from each region to the total June–October burned area.

**Table 3.** Trends and evolution during recent years for the number of days with a CO plumes and with a CO and AOD plumes during June–October. The recent evolution of a given variable $X$ is calculated as the difference between the values averaged over the 2017–2023 period (recent period) minus values averaged over the 2008–2023 period (full period), so that the relative difference is defined as $(\overline{X_{recent}} - \overline{X_{full}})/\overline{X_{full}}$. The symbol * indicates that the trends or the absolute difference $(\overline{X_{recent}} - \overline{X_{full}})$ is significant (p-value<0.1)

| Variable ($X$) | West. Boreal North America | East. Boreal North America | West. Temperate North America | Atlantic | Europe | East. Boreal Asia | East. Central Asia |
|---|---|---|---|---|---|---|---|
| **Number of days with a CO plume in the region during June–October** | | | | | | | |
| Mean 2008–2023 (days.year$^{-1}$) | 21 | 16 | 13 | 17 | 22 | 28 | 19 |
| Trend 2008–2023 (%.year$^{-1}$) | 76.4* | 120.0 | 29.6 | 100.0 | 15.4 | 3.2 | -2.8* |
| Difference recent vs full period (%) | 49.0 | 59.1 | 62.8 | 79.6 | 64.1 | 0.4 | -33.6 |
| **Number of days with a CO and AOD plume in the region during June–October** | | | | | | | |
| Mean 2008–2023 (days.year$^{-1}$) | 9 | 5 | 6 | 4 | 6 | 12 | 5 |
| Trend 2008–2023 (%.year$^{-1}$) | 100* | 266.7 | 28.1 | 22.2* | 95.4 | 1.5 | -8* |
| Difference recent vs full period (%) | 73.5 | 50.6 | 86 | 103.2 | 64.7 | -8.3 | -58.7* |

The number of days with a plume observed increases significantly with the severity of the fire season across mid- and high-latitudes of the Northern Hemisphere. The highest number of plumes was observed during the years 2021 and 2023, with 364 and 462 days, respectively. In contrast, 2022 exhibited the second lowest number of plumes (30 days) and the lowest burned area ($4.1 \times 10^6$ ha).

A significant correlation is found between the total number of days with a detected CO plume in June–October and the total burned area above 30 °N, excluding the Western Central Asia and Western Boreal Asia regions (r = 0.83, p-value = $7.5 \times 10^{-5}$). This suggests that plumes in the Northern Hemisphere are mostly linked to intense wildfires.

From 2017 onwards, the proportion of burned area due to wildfires in the Eastern Central Asia region is very low. Consequently, the variability of fires in that region no longer has an impact on the number of days with a CO plume. Indeed, in accordance with prevailing trends and recent anomalies in CO and AOD, a significant negative trend is observed in the number of days affected by plumes in Eastern Central Asia: -2.9 %.year$^{-1}$ for days with extreme CO plume and -8 %.year$^{-1}$ for simultaneous extreme CO and AOD.

Therefore, since 2017, the interannual variability of the total burned area in latitudes $\geq 30$ °N, excluding the Western Central Asia and Western Boreal Asia regions, appears to be dependent solely on the boreal regions (Eastern Boreal Asia, Western and Eastern Boreal North America) and Western Temperate North America. A large significant positive trend in the number of days with a plume is observed in Western Boreal and Eastern Temperate North America: +72.5 %.year$^{-1}$ and +47.6 %.year$^{-1}$ for CO plumes, and +100 %.year$^{-1}$ and +31.3 %.year$^{-1}$ for simultaneous CO and aerosol plumes. An increase is obtained in the outflow over the Atlantic for simultaneous CO and AOD extremes (+22.2 %.year$^{-1}$). The trends in Eastern Temperate North
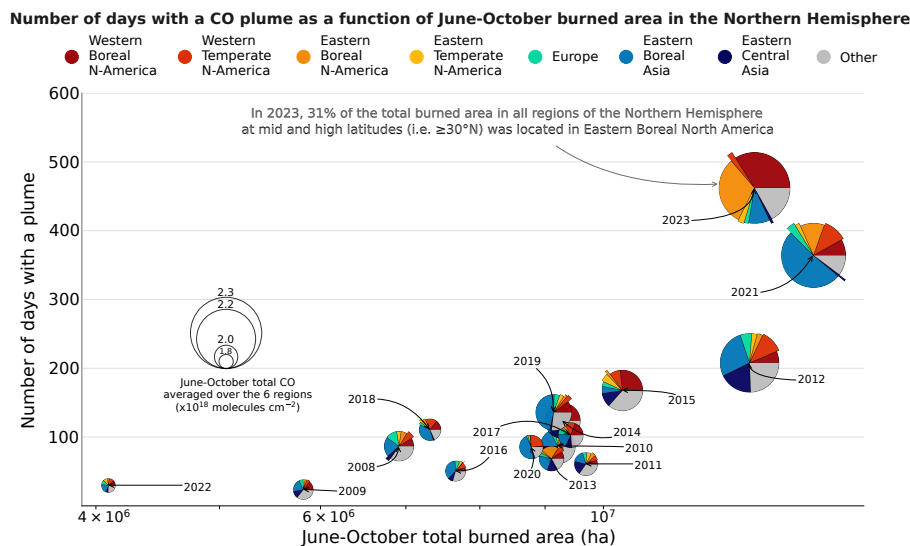
**Figure 11.** Number of days with a detected CO plume in seven regions (Western and Eastern Boreal North America, Western Temperate North America, the Atlantic, Europe, Eastern Boreal Asia and Eastern Central Asia) between June and October and total burned area in the Northern Hemisphere mid and high latitudes ($\geq 30\,°$N), excluding the Western Central Asia and Western Boreal Asia regions, during the same period. The number of days represents the sum of days with a detected plume in each region, which means that a specific day may be counted multiple times. The diameter of each data point corresponds to the average summer CO of the six study regions. The graph also displays the distribution of June–October burned area by region within each data point. This distribution is computed using the total burned area in the Northern Hemisphere mid and high latitudes ($\geq 30\,°$N). The category 'Other' is employed to denote all lands situated within the mid and high latitudes of the Northern Hemisphere ($\geq 30\,°$N) that do not fall within the regions of Western and Eastern Boreal North America, Western Temperate North America, the Atlantic, Europe, Eastern Boreal Asia and Eastern Central Asia.

America and the Atlantic corroborate the impact of transport on CO and AOD, as developed in sections 4.2 and 4.3. An increase by $\simeq 50$ to $100\,\%$ in the number of days with extreme pollution plumes during June–October is also obtained using the difference between 7 recent years (2017-2023) and the whole period studied (2008–2023) in Western and Eastern Boreal North America, Western and Eastern Temperate North America, the Atlantic and Europe (Table 3). It is, however, important to note that in Eastern Boreal Asia, the identification of plumes using extreme values appears to be less reliable, given that there has been a decrease of -1 % and -8.3 % in the number of days with CO plumes and with simultaneous CO and aerosol plumes, respectively. Nevertheless, no significant negative trend was identified. This could be attributed to either the impact of reduced transport from Asia in the region, or to a less reliable plume identification due to the high 97th percentile in this region for both CO and AOD.

A pattern is emerging, with alternating years of intense fires in the aforementioned regions and a high number of plumes (2021, 2023) and years of low fire activity and a low number of plumes (2022). Further updates will be required to confirm the veracity of this pattern.

# 5    Conclusions

This study examines the relationship between fire activity, CO, and AOD, during summer (June–October) in the Northern Hemisphere using 16 years of satellite observations from 2008 to 2023. The results show that intense wildfires have a significant impact on the extreme values of CO and AOD over most of the Northern Hemisphere. The main conclusions for selected regions are summarised in the following.

1. Eastern Central Asia: This region has a high level of fire activity, with large burned area and very frequent fires, suggesting agricultural fires. There is a significant downward trend in the burned area between June and October (-7.8 %.year$^{-1}$). The burned area during that season has decreased in recent years (-71 % for June–October), but the number of intense events is increasing. The observed decrease appears to be due to human intervention rather than a reduction in fire weather risks. There are no summer peaks in CO in this region, indicating a low contribution from fires during that time period. Additionally, a significant and negative trend is observed for June–October mean CO (-0.3 %.year$^{-1}$) as well as for the AOD (-2.1 %.year$^{-1}$). Recent anomalies in CO and AOD are consistently negative, as well as the number of days with a plume. The observed decrease may be explained by a decrease in anthropogenic emissions (including agricultural fires). The negative trends and anomalies in CO and AOD observed during the summer months extend over the majority of the northern mid-latitude Pacific Ocean.

2. Eastern Boreal Asia: The region has experienced a high level of fire activity, resulting in extensive burned areas and intense fires. The extent of burned area during the summer months has increased in recent years, with a +29 % increase observed between June and October. This increase was particularly pronounced during the mid-season, with a +34 % increase observed between July and August. This increase can be attributed to an increase in fire risks, particularly in extreme fire risk, as this region has a positive regional fire weather index 97$^{th}$ percentile trend (+1.0 %.year$^{-1}$). A strong correlation is observed between the mean CO from June to October and the burned area in latitudes $\geq 30\,°$N, with the exclusion of the agricultural regions Western Central Asia and Western Boreal Asia (r = 0.88). A similarly strong correlation is observed between AOD and CO for the months of July and August (r = 0.83). Significant positive trends were observed for both mean and extreme values of CO and AOD at the grid cell scale. Despite the presence of considerable anomalies in extreme values, the number of days with CO plumes and CO combined with aerosol plumes has decreased by -1 % and -8.3 % in Eastern Boreal Asia, respectively. This suggests that the plume detection method may not be entirely reliable for this region.

3. Western Boreal North America, Western Temperate North America: These regions are prone to the occurrence of intense fires, which result in large burned areas. The extent of burned area during the summer months has increased in recent years, with the greatest increase occurring towards the end of the season. For instance, the burned area during June–October has increased by 16 % and 28 %, respectively, while the burned area during September–October has increased by 84 % and 60 %, respectively. This increase can be attributed to a rise in the average and extreme fire risks, particularly towards the end of the season. A positive trend is observed in the regional mean AOD for the June-October period

(+2.4 %.year$^{-1}$) and for both mean and extreme values of CO and AOD at the grid cell scale in Western Boreal North America. In contrast, a negative trend was observed for both mean and extreme values of CO at the gridcell scale in Western Temperate North America. These negative trends are likely due to the reduction in long-range transport of CO from Asia, which is attributed to a decrease in anthropogenic emissions in eastern Asia. In contrast, for aerosols with a shorter lifetime, the reduction in long-range transport from eastern Asia is offset by an increase in regional fire activity. For both regions, a strong correlation between AOD and CO is observed for the months of July–August (r = 0.72 and r = 0.85, respectively). The positive CO and AOD anomalies are consistent with the trend in fire activity, which is confirmed by the strong correlation (r = 0.84 and r = 0.75 respectively) between the June–October mean CO and the burned area in latitudes $\geq$ 30 °N, excluding the agricultural regions Western Central Asia and Western Boreal Asia. These anomalies spread downwind towards the eastern United States and Canada, the Atlantic Ocean, and Europe. In Western Boreal North America, a positive trend in the number of CO plumes (+72.5 %.year$^{-1}$) and CO combined with aerosol plumes (+100 %.year$^{-1}$) is observed. Over the past seven years, the number of days with CO plumes has increased by +51 % and +65.4 % in Western Boreal and Western Temperate North America, respectively. Furthermore, the number of days with CO combined with aerosol plumes has increased by +73.5 % and +86 %, respectively. These two regions are prone to intense wildfires, which are increasing due to larger fire risk, leading to an increase in the extreme values of CO and AOD.

4. Atlantic, Europe: With the exception of the Mediterranean region and Portugal, Europe experiences relatively low levels of fire activity. Over the region, the area burned during the fire season has decreased in recent years, with a reduction of 28 % for the period from June to October. Nevertheless, the number of intense fire events has increased. The observed rise in the frequency of extreme fires is associated with an increase in the probability of extreme fire weather events. This is evidenced by the regional June-October fire weather index, which exhibited a +0.5 % annual increase in trend. Furthermore, these regions are situated in the downwind direction of areas that have experienced an increase in the intensity of wildfires. The rise in extreme values of CO and AOD in these regions, particularly in North America, has led to an increase in extreme values in the Atlantic and in Europe. The June–October mean CO is found to be highly correlated with the burned area in latitudes of 30 °N and above, with the exception of the agricultural regions of Western Central Asia and Western Boreal Asia (r = 0.85 for the Atlantic, r = 0.75 for Europe). The correlation between AOD and CO in July–August is only weakly positive for both regions (r = 0.49 for both), which can be explained by the shorter lifetime of aerosols compared to CO. This results in some CO plumes not being concomitant with aerosol plumes. In the Atlantic, a positive trend in the number of combined CO and aerosol plumes is observed, with an increase of 22 %.year$^{-1}$. Over the past seven years, the number of days with CO plumes has increased by +82 % and +64 % in the Atlantic and Europe, respectively. The increase in the number of days with combined CO and aerosol plumes is even more pronounced, with an increase of +103 % and +65 %, respectively.

5. Human-managed fire regions (Western Boreal and Western Central Asia, Eastern Temperate North America): In agricultural regions, fires are primarily associated with farming practices, are relatively frequent, and exhibit low intensity. The

areas affected by these fires have decreased in recent years (see section 3). Consequently, it is anticipated that these fires will contribute a relatively minor impact to the extremes of CO and AOD (see section 4.4). Indeed, due to the relatively long lifetime of CO, the observed variability in CO throughout the Northern Hemisphere is probably a combination of the impact of increasing fire activity in the different regions. For a more precise analysis of relative contributions, a chemistry-transport model isolating the influence from each region would be necessary. Land cover changes have the potential to modify the CO emissions intensity from fires and the ratios of CO emissions to the burned area in the regions under study. Wang et al. (2020) estimate that in the case of the RCP4.5 scenario, forest areas could increase by up to 20 % in Western Boreal and Western Central Asia and Eastern Temperate North America in 2050 compared with 2000. These regions, which are designated as 'human-managed fire regions' in this study, characterised by less intense fires compared to other study regions, are susceptible to the emergence of extreme forest fires.

This study demonstrates that extreme concentrations of CO and AOD have increased during summer and early fall over most of the Northern Hemisphere due to an increase in intense wildfires in boreal regions and the western United States. For CO, background values also increase during winter. Due to the impact of CO on OH levels, this increase in CO may influence more broadly the oxidizing capacity of the troposphere. The co-emission of methane and other volatile organic compounds by wildfires may also accentuate this effect by decreasing OH (thus increase CO lifetime).

The present study has demonstrated the importance of the impact of recent years on the variables studied. It is important to monitor future years to see if significant trends emerge and if the differences between recent years and the whole period become more pronounced.

The observed increased number of extremes during summer may alter air quality significantly over large areas and offset or slow down the effect of a reduction in anthropogenic emissions. To fully quantify the impact on surface atmospheric pollution, further studies are necessary to characterise the altitude of the observed plumes. Modeling studies would also be required to quantify the production of secondary pollutants within the plumes, their influence on background levels of key pollutants (surface aerosols, ozone) as well as their influence on the oxidizing capacity of the troposphere.

*Code availability.*

*Data availability.* The IASI L2 Carbon Monoxide (CO) Climate Data Record (CDR) data are distributed by EUMETSAT through the EU-METSAT Data Store (http://doi.org/10.15770/EUM_SAF_AC_0047, last access: 7 October 2024). The analysis of fire activity is conducted using MODIS MCD64 and MOD14 products. MCD64A1.061 product is used for burned area, MOD14A1.061 and MYD14A1.061 for active fires. The MODIS MCD64 and MOD14 products were retrieved from the NASA EOSDIS Land Processes Distributed Active Archive Center (LP DAAC), USGS Earth Resources Observation and Science (EROS) Center, Sioux Falls, South Dakota (https://lpdaac.usgs.gov/products/mcd64a1v061/, last access: 7 October 2024, and https://lpdaac.usgs.gov/products/mod14v061/, last access: 7 October 2024). The analysis of aerosol plumes is conducted using MODIS aerosol optical depth products. The MODIS MOD04_L2 and MYD04_L2 products were retrieved

**Table A1.** Relative difference in burned area (%) reported by Jones et al. (2022) for time period 2001–2019 and obtained in this study for 2008–2023. The relative difference is calculated by dividing the absolute difference by the annual mean burned area. The absolute difference in yearly mean regional burned area is calculated by multiplying the yearly mean regional burned area trend (in $1\,000\,\mathrm{km}^2 \cdot \mathrm{year}^{-2}$) by the number of years in the study period (2001-2019 in Jones et al. (2022), 2008-2023 here). Eco-regions Pacific Canadian Forest, Pacific US Forest and East Siberian Forest used by Jones et al. (2022) are compared to Western Boreal North America, Western Temperate North America and Eastern Boreal Asia. * highlights relative differences computed with a significant trends (p<0.05).

|  | Jones et al. (2022) 2001-2019 | This study 2008-2023 |
|---|---|---|
| Pacific Canadian Forest | 63 | 45 |
| Pacific US Forest | 49 | 38 |
| East Siberian Forest | 93 | 69 |
| Boreal North America | 14 | 31 |
| Temperate North America | 42 | 15 |
| Europe | -62* | -46 |
| Boreal Asia | 0.4 | -34 |
| Central Asia | -76* | -97* |

from the NASA EOSDIS Level-1 and Atmosphere Archive & Distribution System Distributed Active Archive Center (LAADS DAAC), Goddard Space Flight Center, Greenbelt, Maryland (https://ladsweb.modaps.eosdis.nasa.gov/missions-and-measurements/products/MOD04_L2, last access: 7 October 2024, and https://ladsweb.modaps.eosdis.nasa.gov/missions-and-measurements/products/MYD04_L2, last access: 7 October 2024). The ERA5 dataset used to compute the fire weather index is the fifth generation atmospheric reanalysis of the global climate produced by the Copernicus Climate Change Service (C3S) at ECMWF and is distributed via the Copernicus Climate Data Store (https://cds.climate.copernicus.eu/datasets/reanalysis-era5-complete?tab=overview, last access: 7 October 2024).

*Code and data availability.*

*Sample availability.*

*Video supplement.*

# Appendix A: Additional figures

**Figure A1.** Regional monthly burned area derived from MODIS for years 2008–2022, for regions mapped in Fig. 1. Note the different y-axis limits between panels.

**Table A2.** Evolution during recent years for key variables of fire weather during time periods June–July, July–August or September–October, over selected regions of the northern hemisphere. The recent evolution of a given variable $X$ is calculated as the difference between the values averaged over the 2017–2023 period (recent period) minus values averaged over the 2008–2023 period (full period), so that the relative difference is defined as $(\overline{X_{recent}} - \overline{X_{full}})/\overline{X_{full}}$. The symbol * indicates that the absolute difference $(\overline{X_{recent}} - \overline{X_{full}})$ is significant (p-value<0.1).

| Variable ($X$) | West. Boreal North America | East. Boreal North America | West. Temperate North America | Europe | East. Boreal Asia | East. Central Asia |
|---|---|---|---|---|---|---|
| **Difference recent vs full period for regional June–October average of Fire Weather Index ($FWI$)** | | | | | | |
| June–July (%) | 1.8 | 11.4 | 1.6 | 4.3 | 6.7 | 2.6 |
| July–August (%) | 3.1 | 9.4 | -0.2 | 1.4 | 5.2 | -7.3 |
| September–October (%) | 4.3 | 14.4 | 1.3 | 3.2 | 4.8 | 1.0 |
| **Difference recent vs full period for regional June–October average of Fire Weather Index ($FWI$) 97th percentile** | | | | | | |
| June–July (%) | -1.8 | -0.9 | -0.5 | 3.4 | 1.1 | 1.3 |
| July–August (%) | 0.9 | -0.5* | 0.1 | 2.8 | -0.1 | -4.1 |
| September–October (%) | 1.2 | -4.9 | 2.2 | -0.4 | 3.6 | 0.6 |
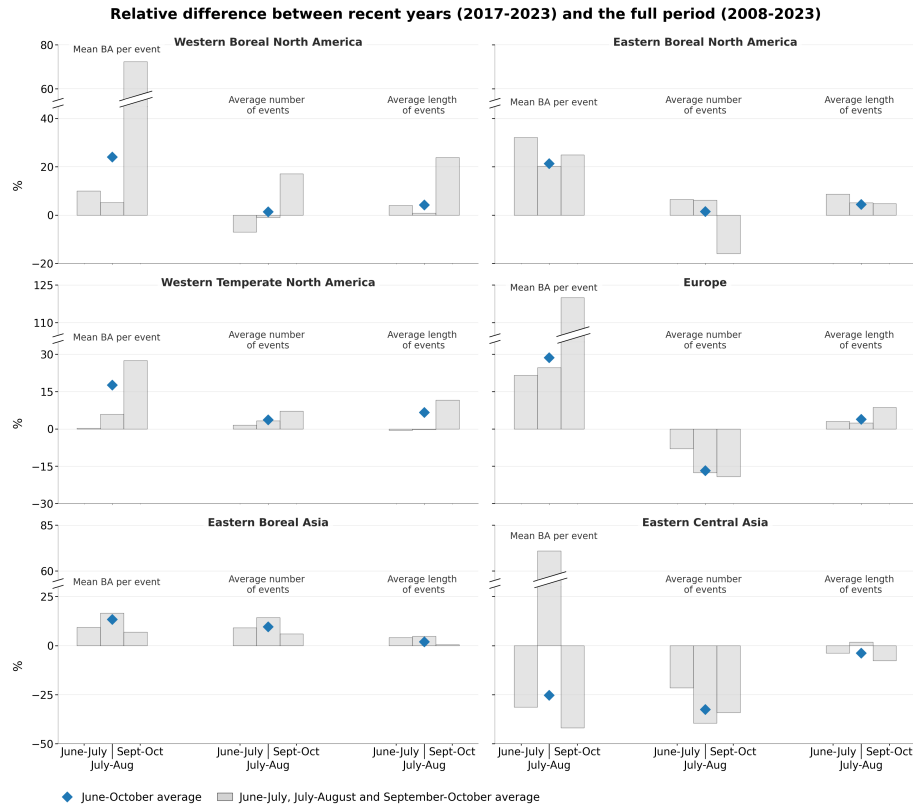
**Figure A2.** Relative difference of the number of events detected in each class of $FRP$ (MW) during recent years (2017–2023) compared to the full period (2008–2023) for the regions mapped in Fig. 1 during time periods June–October, June–July, July–August or September–October. The difference is calculated as (recent-full)/full.
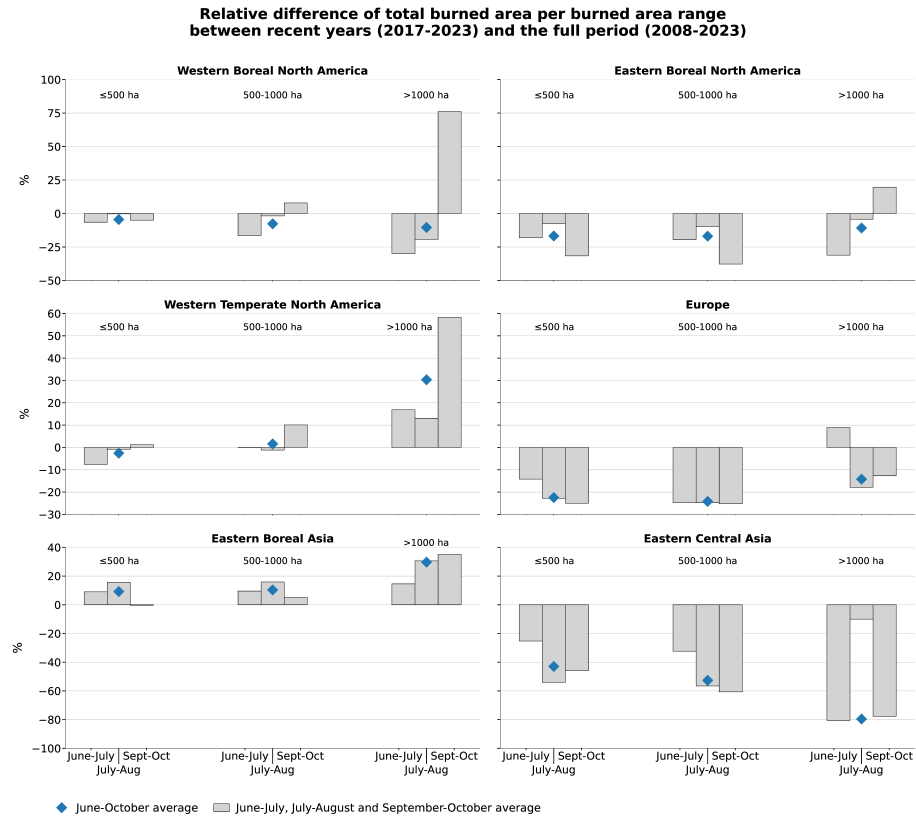
**Figure A3.** Relative difference between recent years (2017–2023) and the full period (2008–2023) of the regional BA, depending on the range of burned area during the fire events (using $BA_e$) during time periods June-October, June-July, July-August or September-October. The difference is calculated as (recent-full)/full.

**Table A3.** Pearson correlation coefficient between different key variables, averaged in selected regions: CO, AOD and total June–October burned area (BA). The total BA corresponds to BA observed above ≥ 30 °N, excluding the Western Central Asia and Western Boreal Asia regions, unless otherwise specified. Only significant correlations (p<0.1) are provided.

| Variable | West. Boreal North America | East. Boreal North America | West. Temperate North America | Atlantic | Europe | East. Boreal Asia | East. Central Asia |
|---|---|---|---|---|---|---|---|
| **Correlation between July-August mean CO and:** | | | | | | | |
| July-August mean AOD | 0.72 | 0.81 | 0.85 | 0.49 | 0.49 | 0.83 | 0.56 |
| **Correlation between June–October mean CO and:** | | | | | | | |
| Total burned area | 0.79 | 0.81 | 0.71 | 0.87 | 0.83 | 0.83 | 0.63 |
| **Correlation between December mean CO and:** | | | | | | | |
| June–October mean CO | 0.43 | 0.72 | – | – | – | – | 0.52 |
| **Correlation between December mean CO and:** | | | | | | | |
| Total burned area | 0.57 | 0.73 | 0.48 | 0.57 | 0.53 | 0.48 | 0.44 |
| **Correlation between June–October monthly number of days with a CO plume per month and:** | | | | | | | |
| Monthly total burned area in Western Boreal North America | 0.63 | 0.77 | 0.21 | 0.63 | 0.54 | 0.38 | 0.28 |
| Monthly total burned area in Western Temperate North America | 0.31 | 0.29 | 0.74 | 0.22 | 0.27 | 0.40 | – |
| Monthly total burned area in Eastern Boreal Asia | 0.66 | 0.45 | 0.55 | 0.31 | 0.25 | 0.75 | 0.29 |
| Monthly total burned area in Eastern Central Asia | -0.25 | -0.21 | -0.2 | – | – | -0.22 | 0.35 |
| Monthly total burned area in Northern Hemisphere > 30 °N | 0.55 | 0.46 | 0.38 | 0.3 | 0.27 | 0.57 | 0.45 |
| Monthly total burned area in Northern Hemisphere > 30 °N without Western Boreal and Central Asia | 0.69 | 0.67 | 0.52 | 0.55 | 0.49 | 0.66 | 0.49 |

*Author contributions.* AE and ST conceptualized the paper and developed the methodology. AE carried out the analysis and designed the figures. AE and ST wrote the original draft. MG, JHL and CC have verified the correct use of the data. AE, ST, MG, JHL and CC reviewed and edited the paper. All authors have read and agreed to the final version of the paper.

*Competing interests.* The contact author has declared that none of the authors has any competing interests.

*Disclaimer.*

*Acknowledgements.* A. Ehret received a grant from CNES. The authors would like to thank CNES for its financial support to the FIRESAT project. IASI is a joint mission of EUMETSAT and the Centre National d'Etudes Spatiales (CNES, France). The authors acknowledge the AERIS data infrastructure for providing access to the IASI data in this study, ULB-LATMOS for the development of the retrieval algorithms, and EUMETSAT/AC SAF for CO data production. The authors acknowledge the LP DAAC (https://lpdaac.usgs.gov/, last access: 7 October 2024), the LAADS DAAC (https://ladsweb.modaps.eosdis.nasa.gov/, last access: 7 October 2024) and the Copernicus Climate Data Store (https://cds.climate.copernicus.eu/, last access: 7 October 2024) for providing MODIS and ERA5 data. The authors would like to thank the ESPRI mesocentre at IPSL for access to computing resources and support in exploiting the data. The authors are grateful to two anonymous referees for their insightful comments.

# References

Aguilera, R., Corringham, T., Gershunov, A., and Benmarhnia, T.: Wildfire smoke impacts respiratory health more than fine particles from other sources: observational evidence from Southern California, Nature Communications, 12, 1493, https://doi.org/10.1038/s41467-021-21708-0, 2021.

Albores, I., Buchholz, R., Ortega, I., Emmons, L., Hannigan, J., Lacey, F., Pfister, G., Tang, W., and Worden, H.: Continental-scale Atmospheric Impacts of the 2020 Western U.S. Wildfires, Atmospheric Environment, 294, 119 436, https://doi.org/10.1016/j.atmosenv.2022.119436, 2023.

Andela, N., Morton, D. C., Giglio, L., Chen, Y., van der Werf, G. R., Kasibhatla, P. S., DeFries, R. S., Collatz, G. J., Hantson, S., Kloster, S., Bachelet, D., Forrest, M., Lasslop, G., Li, F., Mangeon, S., Melton, J. R., Yue, C., and Randerson, J. T.: A Human-Driven Decline in Global Burned Area, Science, 356, 1356–1362, https://doi.org/10.1126/science.aal4108, 2017.

Andreae, M. O.: Emission of trace gases and aerosols from biomass burning – an updated assessment, Atmos. Chem. Phys., 19, 8523–8546, https://doi.org/10.5194/acp-19-8523-2019, 2019.

Andreae, M. O. and Merlet, P.: Emission of trace gases and aerosols from biomass burning, Global Biogeochem. Cycles, 15, 995–966, https://doi.org/10.1029/2000GB001382, 2001.

Barret, B., Loicq, P., Le Flochmoën, E., Bennouna, Y., Hadji-Lazaro, J., Hurtmans, D., and Sauvage, B.: Validation of 12 Years (2008–2019) of IASI-A CO with IAGOS Aircraft Observations, Atmospheric Measurement Techniques, 18, 129–149, https://doi.org/10.5194/amt-18-129-2025, 2025.

Boynard, A., Clerbaux, C., Clarisse, L., Safieddine, S., Pommier, M., Van Damme, M., Bauduin, S., Oudot, C., Hadji-Lazaro, J., Hurtmans, D., and Coheur, P.-F.: First simultaneous space measurements of atmospheric pollutants in the boundary layer from IASI: A case study in the North China Plain, Geophysical Research Letters, 41, 645–651, https://doi.org/10.1002/2013GL058333, _eprint: https://onlinelibrary.wiley.com/doi/pdf/10.1002/2013GL058333, 2014.

Buchholz, R. R., Worden, H. M., Park, M., Francis, G., Deeter, M. N., Edwards, D. P., Emmons, L. K., Gaubert, B., Gille, J., Martinez-Alonso, S., Tang, W., Kumar, R., Drummond, J. R., Clerbaux, C., George, M., Coheur, P.-F. c., Hurtmans, D., Bowman, K. W., Luo, M., Payne, V. H., Worden, J. R., Chin, M., Levy, R. C., Warner, J., Wei, Z., and Kulawik, S. S.: Air pollution trends measured from Terra: CO and AOD over industrial, fire-prone, and background regions, Remote Sensing of Environment, 256, 112 275, https://doi.org/10.1016/j.rse.2020.112275, 2021.

Buchholz, R. R., Park, M., Worden, H. M., Tang, W., Edwards, D. P., Gaubert, B., Deeter, M. N., Sullivan, T., Ru, M., Chin, M., Levy, R. C., Zheng, B., and Magzamen, S.: New seasonal pattern of pollution emerges from changing North American wildfires, Nature Communications, 13, 2043, https://doi.org/10.1038/s41467-022-29623-8, 2022.

Carter, T. S., Heald, C. L., and Selin, N. E.: Large mitigation potential of smoke PM $_{2.5}$ in the US from human-ignited fires, Environmental Research Letters, 18, 014 002, https://doi.org/10.1088/1748-9326/aca91f, 2023.

Ceamanos, X., Coopman, Q., George, M., Riedi, J., Parrington, M., and Clerbaux, C.: Remote sensing and model analysis of biomass burning smoke transported across the Atlantic during the 2020 Western US wildfire season, Sci Rep, 13, 16 014, https://doi.org/10.1038/s41598-023-39312-1, 2023.

Chen, G., Guo, Y., Yue, X., Tong, S., Gasparrini, A., Bell, M. L., Armstrong, B., Schwartz, J., Jaakkola, J. J. K., Zanobetti, A., Lavigne, E., Nascimento Saldiva, P. H., Kan, H., Royé, D., Milojevic, A., Overcenco, A., Urban, A., Schneider, A., Entezari, A., Vicedo-Cabrera, A. M., Zeka, A., Tobias, A., Nunes, B., Alahmad, B., Forsberg, B., Pan, S.-C., Íñiguez, C., Ameling, C., De la Cruz Valencia, C., Åström,

730    C., Houthuijs, D., Van Dung, D., Samoli, E., Mayvaneh, F., Sera, F., Carrasco-Escobar, G., Lei, Y., Orru, H., Kim, H., Holobaca, I.-H., Kyselý, J., Teixeira, J. P., Madureira, J., Katsouyanni, K., Hurtado-Díaz, M., Maasikmets, M., Ragettli, M. S., Hashizume, M., Stafoggia, M., Pascal, M., Scortichini, M., de Sousa Zanotti Stagliorio Coêlho, M., Valdés Ortega, N., Ryti, N. R. I., Scovronick, N., Matus, P., Goodman, P., Garland, R. M., Abrutzky, R., Garcia, S. O., Rao, S., Fratianni, S., Dang, T. N., Colistro, V., Huber, V., Lee, W., Seposo, X., Honda, Y., Guo, Y. L., Ye, T., Yu, W., Abramson, M. J., Samet, J. M., and Li, S.: Mortality risk attributable to wildfire-related PM2·5 pollution: a global time series study in 749 locations, The Lancet Planetary Health, 5, e579–e587, https://doi.org/10.1016/S2542-735    5196(21)00200-X, 2021a.

Chen, Y., Romps, D. M., Seeley, J. T., Veraverbeke, S., Riley, W. J., Mekonnen, Z. A., and Randerson, J. T.: Future increases in Arctic lightning and fire risk for permafrost carbon, Nature Climate Change, 11, 404–410, https://doi.org/10.1038/s41558-021-01011-y, 2021b.

Chen, Y., Hall, J., van Wees, D., Andela, N., Hantson, S., Giglio, L., van der Werf, G. R., Morton, D. C., and Randerson, J. T.: Multi-decadal trends and variability in burned area from the fifth version of the Global Fire Emissions Database (GFED5), Earth System Science Data, 740    15, 5227–5259, https://doi.org/10.5194/essd-15-5227-2023, publisher: Copernicus GmbH, 2023.

Clerbaux, C., Boynard, A., Clarisse, L., George, M., Hadji-Lazaro, J., Herbin, H., Hurtmans, D., Pommier, M., Razavi, A., Turquety, S., Wespes, C., and Coheur, P.-F.: Monitoring of atmospheric composition using the thermal infrared IASI/MetOp sounder, Atmospheric Chemistry and Physics, 9, 6041–6054, https://doi.org/10.5194/acp-9-6041-2009, 2009.

Edwards, D. P., Emmons, L. K., Hauglustaine, D. A., Chu, D. A., Gille, J. C., Kaufman, Y. J., Pétron, G., Yurganov, L. N., Giglio, 745    L., Deeter, M. N., Yudin, V., Ziskin, D. C., Warner, J., Lamarque, J.-F., Francis, G. L., Ho, S. P., Mao, D., Chen, J., Grechko, E. I., and Drummond, J. R.: Observations of carbon monoxide and aerosols from the Terra satellite: Northern Hemisphere variability, https://doi.org/10.1029/2004JD004727, 2004.

Ford, B., Val Martin, M., Zelasky, S. E., Fischer, E. V., Anenberg, S. C., Heald, C. L., and Pierce, J. R.: Future Fire Impacts on Smoke Concentrations, Visibility, and Health in the Contiguous United States, GeoHealth, 2, 229–247, https://doi.org/10.1029/2018GH000144, 750    2018.

Giglio, L., Csiszar, I., and Justice, C. O.: Global distribution and seasonality of active fires as observed with the Terra and Aqua Moderate Resolution Imaging Spectroradiometer (MODIS) sensors, Journal of Geophysical Research: Biogeosciences, 111, https://doi.org/10.1029/2005JG000142, 2006.

Giglio, L., Randerson, J. T., van der Werf, G. R., Kasibhatla, P. S., Collatz, G. J., Morton, D. C., and DeFries, R. S.: Assessing variability and 755    long-term trends in burned area by merging multiple satellite fire products, Biogeosciences, 7, 1171–1186, https://doi.org/10.5194/bg-7-1171-2010, 2010.

Giglio, L., Justice, C., Boschetti, L., and Roy, D.: MCD64A1 MODIS/Terra+Aqua Burned Area Monthly L3 Global 500m SIN Grid V006, https://doi.org/doi: 10.5067/MODIS/MCD64A1.006, 2015.

Giglio, L., Boschetti, L., Roy, D. P., Humber, M. L., and Justice, C. O.: The Collection 6 MODIS burned area mapping algorithm and product, 760    Remote Sensing of Environment, 217, 72 – 85, https://doi.org/https://doi.org/10.1016/j.rse.2018.08.005, 2018.

Grillakis, M., Voulgarakis, A., Rovithakis, A., Seiradakis, K. D., Koutroulis, A., Field, R. D., Kasoar, M., Papadopoulos, A., and Lazaridis, M.: Climate drivers of global wildfire burned area, Environmental Research Letters, 17, 045 021, https://doi.org/10.1088/1748-9326/ac5fa1, 2022.

Hall, J., Argueta, F., Zubkova, M., Chen, Y., Randerson, J., and Giglio, L.: GloCAB: Global Cropland Burned Area from Mid-2002 to 2020, 765    https://doi.org/10.5194/essd-16-867-2024, 2024.

Hessilt, T. D., Abatzoglou, J. T., Chen, Y., Randerson, J. T., Scholten, R. C., Werf, G. v. d., and Veraverbeke, S.: Future increases in lightning ignition efficiency and wildfire occurrence expected from drier fuels in boreal forest ecosystems of western North America, Environmental Research Letters, 17, 054 008, https://doi.org/10.1088/1748-9326/ac6311, 2022.

Hurtmans, D., Coheur, P.-F., Wespes, C., Clarisse, L., Scharf, O., Clerbaux, C., Hadji-Lazaro, J., George, M., and Turquety, S.: FORLI radiative transfer and retrieval code for IASI, JQSRT, 113, 1391–1408, https://doi.org/10.1016/j.jqsrt.2012.02.036, 2012.

Hussain, M. and Mahmud, I.: pyMannKendall: a python package for non parametric Mann Kendall family of trend tests, https://doi.org/10.21105/joss.01556, 2019.

Intergovernmental Panel On Climate Change: Climate Change 2021 – The Physical Science Basis: Working Group I Contribution to the Sixth Assessment Report of the Intergovernmental Panel on Climate Change, Cambridge University Press, 1 edn., ISBN 978-1-00-915789-6, https://doi.org/10.1017/9781009157896, 2023.

Jaffe, D., Hafner, W., Chand, D., Westerling, A., and Spracklen, D.: Inter-annual Variations in PM2.5 due to Wildfires in the Western United States, Environmental Science and Technology, 42, 2812–2818, https://doi.org/10.1021/es702755v, 2008.

Jain, P., Castellanos-Acuna, D., Coogan, S. C. P., Abatzoglou, J. T., and Flannigan, M. D.: Observed increases in extreme fire weather driven by atmospheric humidity and temperature, Nature Climate Change, 12, 63–70, https://doi.org/10.1038/s41558-021-01224-1, 2022.

Johnston, F. H., Henderson, S. B., Chen, Y., Randerson, J. T., Marlier, M., DeFries, R. S., Kinney, P., Bowman, D. M., and Brauer, M.: Estimated Global Mortality Attributable to Smoke from Landscape Fires, Environmental Health Perspectives, 120, 695–701, https://doi.org/10.1289/ehp.1104422, 2012.

Jolly, W. M., Cochrane, M. A., Freeborn, P. H., Holden, Z. A., Brown, T. J., Williamson, G. J., and Bowman, D. M. J. S.: Climate-induced variations in global wildfire danger from 1979 to 2013, Nature Communications, 6, 7537, https://doi.org/10.1038/ncomms8537, 2015.

Jones, M. W., Abatzoglou, J. T., Veraverbeke, S., Andela, N., Lasslop, G., Forkel, M., Smith, A. J. P., Burton, C., Betts, R. A., Van Der Werf, G. R., Sitch, S., Canadell, J. G., Santín, C., Kolden, C., Doerr, S. H., and Le Quéré, C.: Global and Regional Trends and Drivers of Fire Under Climate Change, Reviews of Geophysics, 60, e2020RG000 726, https://doi.org/10.1029/2020RG000726, 2022.

Karanasiou, A., Alastuey, A., Amato, F., Renzi, M., Stafoggia, M., Tobias, A., Reche, C., Forastiere, F., Gumy, S., Mudu, P., and Querol, X.: Short-term health effects from outdoor exposure to biomass burning emissions: A review, Science of The Total Environment, 781, 146 739, https://doi.org/10.1016/j.scitotenv.2021.146739, 2021.

Keywood, M., Cope, M., Meyer, C. P. M., Iinuma, Y., and Emmerson, K.: When smoke comes to town: The impact of biomass burning smoke on air quality, 121, 13–21, https://doi.org/https://doi.org/10.1016/j.atmosenv.2015.03.050, 2015.

Langerock, B.: Validation report of reprocessed IASI L2 CO CDR for Metop-A and B, Tech. Rep. AF/AC/IASI/VR/IASI_CO_CDR_L2, EumetSAT, 2023.

Laurent, P., Mouillot, F., Moreno, M. V., Yue, C., and Ciais, P.: Varying relationships between fire radiative power and fire size at a global scale, https://doi.org/10.5194/bg-16-275-2019, 2019.

Levy, R. C., Mattoo, S., Munchak, L. A., Remer, L. A., Sayer, A. M., Patadia, F., and Hsu, N. C.: The Collection 6 MODIS aerosol products over land and ocean, Atmospheric Measurement Techniques, 6, 2989–3034, https://doi.org/10.5194/amt-6-2989-2013, 2013.

Levy, R. C., Hsu, C., et al.: MODIS Atmosphere L2 Aerosol Product. NASA MODIS Adaptive Processing System, Goddard Space Flight Center, https://doi.org/http://dx.doi.org/10.5067/MODIS/MOD04_L2.006, 2015.

Lizundia-Loiola, J., Franquesa, M., Khairoun, A., and Chuvieco, E.: Global burned area mapping from Sentinel-3 Synergy and VIIRS active fires, Remote Sensing of Environment, 282, 113 298, https://doi.org/10.1016/j.rse.2022.113298, 2022.

McElhinny, M., Beckers, J. F., Hanes, C., Flannigan, M., and Jain, P.: A high-resolution reanalysis of global fire weather from 1979 to 2018 – overwintering the Drought Code, Earth System Science Data, 12, 1823–1833, https://doi.org/10.5194/essd-12-1823-2020, 2020.

805 O'Dell, K., Ford, B., Fischer, E. V., and Pierce, J. R.: Contribution of Wildland-Fire Smoke to US PM2.5 and Its Influence on Recent Trends, Environmental Science & Technology, 53, 1797–1804, https://doi.org/10.1021/acs.est.8b05430, 2019.

Parisien, M.-A., Barber, Q. E., Bourbonnais, M. L., Daniels, L. D., Flannigan, M. D., Gray, R. W., Hoffman, K. M., Jain, P., Stephens, S. L., Taylor, S. W., and Whitman, E.: Abrupt, climate-induced increase in wildfires in British Columbia since the mid-2000s, Communications Earth & Environment, 4, 309, https://doi.org/10.1038/s43247-023-00977-1, 2023.

810 Ramo, R., Roteta, E., Bistinas, I., van Wees, D., Bastarrika, A., Chuvieco, E., and van der Werf, G. R.: African burned area and fire carbon emissions are strongly impacted by small fires undetected by coarse resolution satellite data, Proceedings of the National Academy of Sciences, 118, e2011160 118, https://doi.org/10.1073/pnas.2011160118, publisher: Proceedings of the National Academy of Sciences, 2021.

Randerson, J. T., Chen, Y., van der Werf, G. R., Rogers, B. M., and Morton, D. C.: Global burned area and biomass burning emissions from 815 small fires, Journal of Geophysical Research: Biogeosciences, 117, https://doi.org/10.1029/2012JG002128, 2012.

San-Miguel-Ayanz, J., Durrant, T., Boca, R., Maianti, P., Liberta', G., Jacome, F. O. D., Branco, A., De, R. D., Suarez-Moreno, M., Ferrari, D., Roglia, E., Scionti, N., Broglia, M., Onida, M., Tistan, A., and Loffler, P.: Forest Fires in Europe, Middle East and North Africa 2023, Publications Office of the European Union, JRC139704, https://doi.org/10.2760/8027062, 2024.

Sayer, A. M., Munchak, L. A., Hsu, N. C., Levy, R. C., Bettenhausen, C., and Jeong, M.-J.: MODIS Collection 6 aerosol products: Compar-820 ison between Aqua's e-Deep Blue, Dark Target, and "merged" data sets, and usage recommendations, Journal of Geophysical Research: Atmospheres, 119, 13,965–13,989, https://doi.org/https://doi.org/10.1002/2014JD022453, 2014.

Scholten, R. C., Jandt, R., Miller, E. A., Rogers, B. M., and Veraverbeke, S.: Overwintering fires in boreal forests, Nature, 593, 399–404, https://doi.org/10.1038/s41586-021-03437-y, 2021.

Spracklen, D., Logan, J., Mickley, L., Park, R., Yevich, R., Westerling, A., and Jaffe, D.: Wildfires drive interannual variability of organic 825 carbon aerosol in the western U.S. in summer, Geophysical Research Letters, 34, https://doi.org/10.1029/2007GL030037, 2007.

Szopa, S., Hauglustaine, D. A., and Ciais, P.: Relative contributions of biomass burning emissions and atmospheric transport to carbon monoxide interannual variability, Geophysical Research Letters, 34, https://doi.org/10.1029/2007GL030231, 2007.

Tian, C., Yue, X., Zhu, J., Liao, H., Yang, Y., Chen, L., Zhou, X., Lei, Y., Zhou, H., and Cao, Y.: Projections of fire emissions and the consequent impacts on air quality under 1.5 °C and 2 °C global warming, Environmental Pollution, 323, 121 311, 830 https://doi.org/10.1016/j.envpol.2023.121311, 2023.

Turquety, S., Menut, L., Siour, G., Mailler, S., Hadji-Lazaro, J., George, M., Clerbaux, C., Hurtmans, D., and Coheur, P.-F.: APIFLAME v2.0 biomass burning emissions model: impact of refined input parameters on atmospheric concentration in Portugal in summer 2016, Geoscientific Model Development, 13, 2981–3009, https://doi.org/10.5194/gmd-13-2981-2020, 2020.

van Marle, M. J. E., Kloster, S., Magi, B. I., Marlon, J. R., Daniau, A.-L., Field, R. D., Arneth, A., Forrest, M., Hantson, S., Kehrwald, N. M., 835 Knorr, W., Lasslop, G., Li, F., Mangeon, S., Yue, C., Kaiser, J. W., and van der Werf, G. R.: Historic global biomass burning emissions for CMIP6 (BB4CMIP) based on merging satellite observations with proxies and fire models (1750–2015), Geoscientific Model Development, 10, 3329–3357, https://doi.org/10.5194/gmd-10-3329-2017, 2017.

Van Wagner, C.: Development and structure of the Canadian forest fire weather index system, Canadian Forestry Service, Ottawa, Technical Report 35, 1987.

840    Veraverbeke, S., Rogers, B. M., Goulden, M. L., Jandt, R. R., Miller, C. E., Wiggins, E. B., and Randerson, J. T.: Lightning as a major driver of recent large fire years in North American boreal forests, Nature Climate Change, 7, 529–534, https://doi.org/10.1038/nclimate3329, 2017.

Wang, L., Tai, A. P. K., Tam, C.-Y., Sadiq, M., Wang, P., and Cheung, K. K. W.: Impacts of Future Land Use and Land Cover Change on Mid-21st-Century Surface Ozone Air Quality: Distinguishing between the Biogeophysical and Biogeochemical Effects, Atmospheric

845    Chemistry and Physics, 20, 11 349–11 369, https://doi.org/10.5194/acp-20-11349-2020, 2020.

Wang, S., Yin, C., Li, F., and Richel, A.: Innovative Incentives Can Sustainably Enhance the Achievement of Straw Burning Control in China, 857, 159 498, https://doi.org/10.1016/j.scitotenv.2022.159498, 2023.

Wooster, M. J. and Zhang, Y. H.: Boreal Forest Fires Burn Less Intensely in Russia than in North America, Geophysical Research Letters, 31, https://doi.org/10.1029/2004GL020805, 2004.

850    Xu, R., Yu, P., Abramson, M. J., Johnston, F. H., Samet, J. M., Bell, M. L., Haines, A., Ebi, K. L., Li, S., and Guo, Y.: Wildfires, Global Climate Change, and Human Health, New England Journal of Medicine, 383, 2173–2181, https://doi.org/10.1056/NEJMsr2028985, 2020.

Zheng, B., Chevallier, F., Ciais, P., Yin, Y., Deeter, M. N., Worden, H. M., Wang, Y., Zhang, Q., and He, K.: Rapid decline in carbon monoxide emissions and export from East Asia between years 2005 and 2016, Environmental Research Letters, 13, 044 007, https://doi.org/10.1088/1748-9326/aab2b3, 2018.

855    Zheng, B., Chevallier, F., Yin, Y., Ciais, P., Fortems-Cheiney, A., Deeter, M. N., Parker, R. J., Wang, Y., Worden, H. M., and Zhao, Y.: Global atmospheric carbon monoxide budget 2000–2017 inferred from multi-species atmospheric inversions, Earth System Science Data, 11, 1411–1436, https://doi.org/10.5194/essd-11-1411-2019, 2019.

Zhuang, Y., Li, R., Yang, H., Chen, D., Chen, Z., Gao, B., and He, B.: Understanding Temporal and Spatial Distribution of Crop Residue Burning in China from 2003 to 2017 Using MODIS Data, 10, 390, https://doi.org/10.3390/rs10030390, 2018.